Linear Optical Characterization of Graphene Structure

By

Jing Xu

A thesis

presented to the University of Waterloo

in fulfillment of the

thesis requirement for the degree of

Master of Applied Science

in

Electrical and Computer Engineering

Waterloo, Ontario, Canada, 2018

I hereby declare that I am the sole author of this thesis. This is a true copy of the thesis, including any required final revisions, as accepted by my examiners.

I understand that my thesis maybe made electronically available to the public.

.

Abstract

Graphene as a newly developed 2D material has attracted a lot of attention for its promising applications in optoelectronic fields. To pursue a profound understanding of its optical properties, this thesis presents the optical refractive index in response to the infrared incidents, and its modulations under external electric field.

We tested the optical reflection response of monolayer graphene on an SiO_2/Si substrate at 1550nm laser incident. The derived value of the graphene optical refractive index was: $2.75 - 1.56i$ at 1550nm, which made up for the deficiency of graphene optical properties in the infrared region. We also compared the results for the current work with studies in the visible spectrum, and we provide a value range for graphene RI, which can be used to estimate the monolayer graphene optical response to different incidents and substrates. Finally, we checked the graphene optical reflection changes in response to an external electric field using a top-gated graphene samples at 1064nm incident. We found that the tunability of complex refractive index of graphene verified according to gate voltage. Additionally, through comparison with other experimental work, we have found the optical refractive index trends are similar in infrared range.

Acknowledgements

I am deeply grateful to my supervisor, Prof. A. H. Majedi, for his kind guidance and excellent supervision. His knowledge and expertise in the field of device technology and especially graphene devices added considerably to my graduate experience. I would really like to appreciate his invaluable help and friendship.

I am heartily thankful to my colleague Behrooz Semnani for his sincere help of theoretical model of the project.

I would like to express my deep gratitude to Sidd Thakur for his help on my experiment setup build.

I am thankful to Dr. Mohsen Raeiszadeh for his kind support and guidance in the fabrication part.

Many Thanks are given to my friend Claude Ciravi for his help and fruitful discussions during the thesis writing.

I thank my family for all supports and inspiration they have been giving me for all my life.

Tables of Contents

List of Figures

List of Tables

List of symbols

$\overrightarrow{a_1}, \overrightarrow{a_2}$	Two primitive lattice vectors
a	The nearest carbon atoms distance in graphene $a \approx 1.42\text{Å}$
σ	Optical conductivity
$\vec{k}$	Incident wave vector
ω	Incident frequency
A	Material absorptance
$\hat{H}$	Hamiltonian of band structure
$\vec{E}$	Electrical field
$\vec{D}$	Electrical displacement
$\vec{H}$	Magnetic field
φ_h	Occupied hole states in band structure
φ_e	Empty electron states in band structure
$\mathcal{E}$	Photon energy
c	Light speed in air
ε_0	The free space permittivity $\varepsilon_0 = 8.854 \times 10^{-12} F/m$
ε_r	Relative permittivity
μ_0	The free space magnetic permeability $\mu_0 = 4\pi \times 10^{-7} H/m$
μ_r	Relative permeability of material
n_g	Optical refractive index of graphene
ω_0	The Gaussian beam-waist
$\omega(z)$	Gaussian beam spot width, function of the distance z along the beam
$\mathrm{R(z)}$	The radius of curvature of the wavefront, $\mathrm{R(z)} = \mathrm{z} + \frac{z_R^2}{z}$
z_R	constant Raleigh range of a beam
M^2	Laser beam quality factor
θ_0	Gaussian beam divergence angle
ϕ_k	Electromagnetic field phase in medium
d_k	The thickness of dielectric medium
n_k	Refractive index of dielectric medium
r	reflection coefficient
R	Reflectivity
t	Transmitance coefficient
T	Transmitivity
n_g'	Real part of graphene refractive index
k_g	Imaginary part of graphene refractive index
J_k	Surface current generated on dielectric medium
e	Tthe electron elementary charge
k_B	The Boltzmann Constant

T	temparature unit Kelvin
Γ	Landau level index dependent scattering rate, a constant $\hbar\Gamma = 0.1\text{eV}$;
$\hbar$	Reduced Planck's Constant $\hbar = \frac{h}{2\pi}$
μ_c	the chemical energy potential of the band structure.
g_v	valley degeneracy factors of graphene band structure $g_v = 2$
g_s	spin degeneracy factors of graphene $g_s = 2$
$f_d(\varepsilon)$	Fermi-Dirac distribution $f_d(\varepsilon) = \left(e^{(\varepsilon-\mu_c)/k_BT} + 1\right)^{-1}$
v_F	The Fermi velocity
γ_2	The frequency dependent impurity scattering rate
E_f	Fermi energy
n_s	Charge carrier density
C_{SiO_2}	The gate capacitance per unit area of the gated graphene sample
V_D	Dirac voltage
V_G	Applied Gate voltage
I_{SD}	Source-Drain current on gated graphene
d_g	Thickness of graphene
λ	Incident wavelength.
β_{ox}	The propagation constant of the SiO_2 layer

1 Introduction

Since its discovery (in 2004), graphene, as a new two-dimensional material, has attracted many researchers' attention. Known as the thinnest elastic material, it is valued for its outstanding electrical, mechanical, optical and thermal properties [1-7]. Graphene, a so-called "wonder material", will compliment the current semiconductor materials and be a central part in future devices, as it is lighter, stronger, more flexible and higher sensitive to electrons and photons.

In 1947, P. R. Wallace started the theoretical research on graphite band structure. Then in the early 1970s, single layers of graphite were epitaxially grown on top of SiC and other semi-conductive materials. The breakthrough happened in 2004 when André Geim and Konstantin Novoselov successfully isolated a single atomic thin layer of graphite with adhesive tape [8]. Since its discovery, great interest has grown in developing the large-scale production of graphene, and in unveiling its properties in preparing, detecting, transferring, characters, and control fields. These properties have inspired a wide variety of technological applications, spurred on by potential applications such as single-electron transistors [1], flexible displays [2], and solar cells [4]. A lot of research effort devoted to understanding the main physical properties of graphene.

1.1 Research motivation

The electronic properties of graphene, i.e., the significant mobility of its massless electrons/holes (due to linear dispersive band structure) and its two-dimensional systems (monolayer structure), give it advantages over other semiconductor materials [5, 6].Thanks to the linear dispersion relation, the density of states in graphene are proportional to the energy, which creates a high density of electrons and holes. When graphene is introduced in field-effect transistors (FETs) as the channel material, it will exceed the limits on conventional planar transistor performance, so that it will giving a role booster technology for making short-channel-free ultimately fast transistors.

Let us consider the optoelectronic properties of graphene. In addition to being conductive and transparent, the next generation of optoelectronic devices requires that transparent conductive electrodes be lightweight, flexible, cheap, and compatible with large-scale fabricating methods. As the most-transparent material (with a transmittance of around 98% per layer), and due to its universal conductivity, graphene has an excellent potential for the electrode application of organic electronic devices where low sheet resistance and high transparency are essential [9].

The elementary condition needed to achieve the technology applications of graphene is appropriately understanding of its optical and electronic properties. The research described in the optical refractive index of monolayer graphene in response to infrared incidents and how the optical properties change due to manipulation of external gated voltages.

1.2 Thesis objective and contribution

In the past few years, the researches in graphene optical properties area has concentrated on the visible range. However, the optical response of graphene under infrared region is a deficiency. To supplement the lack, the primary purpose of the thesis is obtaining the refractive index of graphene at the infrared range, and the influences of external voltage on it.

This is the first time we report the refractive index (RI) of graphene under infrared incidents. Also, we present an evaluation method of graphene (RI) with different incidents wavelengths. Combined the results of optical reflection experiments and the evaluation method, we derived the complex value of graphene RI and compared it with reported ones. Besides, we tested how graphene RI transforms with external gate voltage changing.

1.3 Outline

This thesis presents the linear complex optical refractive index of monolayer graphene and its tunability with electrical control.

Chapter 2 describes the introduction of the atomic structure of graphene, and related electronic, mechanical, optical properties and transport with external fields. Then several opto-electronic applications are submitted due to the unique properties. In Chapter 3, we present the synthesis of monolayer graphene samples and the preparation procedure of gated graphene samples in our experiments. Chapter 4 is the experimental part. In this section, we obtained the reflectivity data through the optical reflection tests and calculated the value of graphene refractive index, then compare the results with ones in literatures. In the last chapter, we summarize the whole work and draw conclusions.

2 Introduction to graphene

Carbon materials, which are entirely composed of carbon, have various allotropes. In nature, graphite and diamond are the bulk allotrope of carbon. From the last decades, a serial of novel nanostructures of carbon allotropes has been discovered. They include Fullerene, Carbon nanotubes, and graphene [10]. The atomic structure of these carbon allotropes is sketched in Figure 2.1.

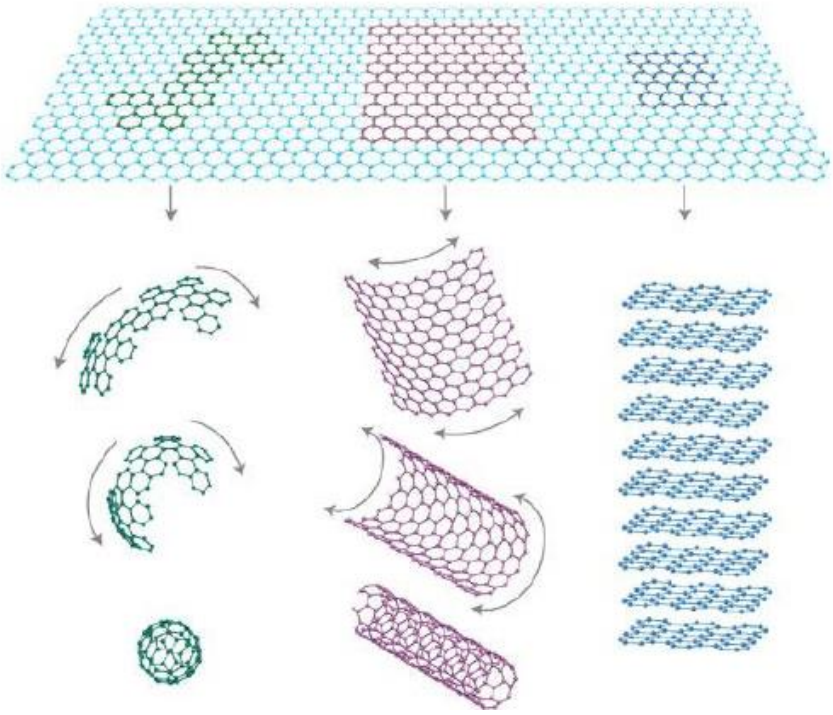

Figure 2.1 Schematic of carbon family materials (a) Bulky ball, (b) Carbon nanotube. (c) Graphene [10].

2.1 Graphene atomic structure

Graphene, the name given to a flat monolayer of carbon atoms tightly packed into a two-dimensional (2D) honeycomb lattice, is a fundamental building block for graphitic materials of all other dimensionalities (shown as in Figure 2.2). It has fascinating electronic, optical and mechanical properties and these properties, which are attracting attention for both scientific research as well as engineering applications.

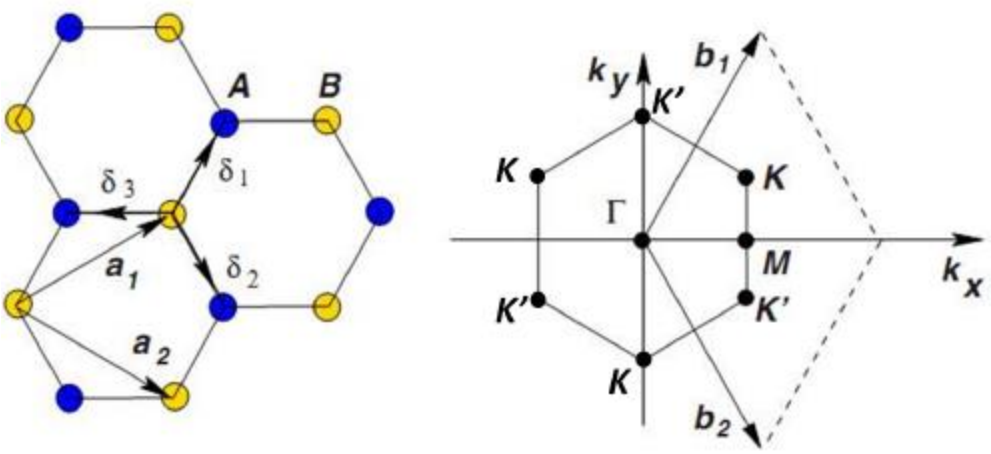

Figure 2.2 Graphene lattice structure and its Brillouin zone [11]

In the structure in Figure 2.2 a, there are two non-equivalent atoms in each unit cell (the area enclosed by dashed lines), named the A atom and B atom, respectively. Two primitive lattice vectors are forming an angle of 60 degrees. Based on these two natural lattice vectors ($\overrightarrow{a_1}, \overrightarrow{a_2}$), the first Brillouin Zone (Figure 2.2 b) can be derived as momentum space. Reciprocal wave vectors connect three of the six corners in the first Brillouin zone, so they are equivalent and named as *K* points. The other three equal points are designated as *K'* point (see Figure 2.2).

This lattice structure can be simulated with a tight binding model, with the lattice vectors (shown in Figure 2.1 a):

$$\overrightarrow{a_1} = \frac{a}{2}\left(3,\ \sqrt{3}\right)\ , \qquad \overrightarrow{a_2} = \frac{a}{2}\left(3, -\sqrt{3}\right) \tag{2-1}$$

Where $a \approx 1.42\text{Å}$ is the nearest neighbor distance. It corresponds to a so-called conjugated carbon bond (like in benzene) intermediate between a single bond and a double bond, with lengths $r_1 \approx 1.54\text{Å}$, and $r_2 \approx 1.31\text{Å}$, respectively. Atoms A and B belong to two different sublattices, and each atom from sublattices A being surrounded by three atoms from sublattices B, and vice versa. The reciprocal lattice is derive in the same way the lattice vectors $(\overrightarrow{b_1}, \overrightarrow{b_2})$ in Brillouin zone.

$$\overrightarrow{b_1} = \frac{2\pi}{3a}\left(1, \sqrt{3}\right), \quad \overrightarrow{b_2} = \frac{2\pi}{3a}\left(1, -\sqrt{3}\right) \tag{2-2}$$

In the nearest neighbour approximation, there is no hopping process within the sub-lattices; hopping occurs only between A and B. The tight binding Hamiltonian is therefore described by the 2×2 matrix [10]

$$\hat{H}\left(\vec{k}\right) = \begin{pmatrix} 0 & tS\left(\vec{k}\right) \\ tS^*\left(\vec{k}\right) & 0 \end{pmatrix} \tag{2-3}$$

Where *t* is the hopping parameter, $\vec{k} = (k_x, k_y)$ is the electrons wave vector and

$$S\left(\vec{k}\right) = 2\exp\left(\frac{ik_x a}{2}\right)\cos\left(\frac{k_y a\sqrt{3}}{2}\right) + \exp(-ik_x a) \tag{2-4}$$

Near these points, charge carriers have a linear dispersion, unlike the parabolic dispersion is other 2D electron gas systems. This results in conical valence and conduction bands touching each other at the Dirac points. (Figure 2.3) Thus, graphene can be considered as a zero-gap semiconductor with a linear dispersion governed by the Dirac equation, this equation is often used to describe the dispersion of light and massless relativistic particles.

$$E(k)_{\pm} = \pm h v_f |k| \tag{2-5}$$

Where h is the Plank constant, and v_f is Fermi velocity.

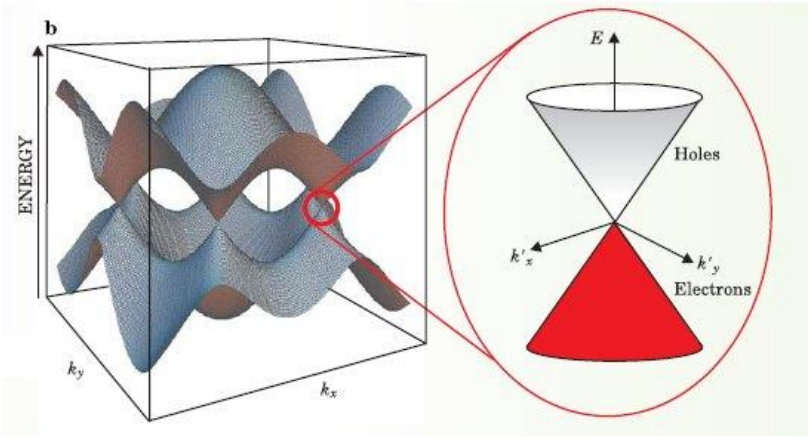

Figure 2.3 Electronic band structure of graphene at Dirac points [10]

2.2 Graphene as a 2D material

2.2.1 Electronic properties of graphene

The electronic properties of graphene results from its low-dimensional structure. As explained in section 2.1, the honeycomb lattice structure of graphene is made up of three unit cells with two unequavalent atoms. Thus, a tight-binding approximation [12] is used to describe the electronic structure of graphene. Solving the Hamiltonian equation of graphene structure (equations (2-3), (2-4)) derives the energy dispersion relation:

$$\varepsilon(k_x, k_y) = \pm t\sqrt{1 + 4\cos\left(\frac{\sqrt{3}k_x a}{2}\right)cos\left(\frac{k_y a}{2}\right) + 4\left[cos\left(\frac{k_y a}{2}\right)\right]^2} \tag{2-6}$$

Where k_x and k_y are the x and y components of the k vector (shown in Figure 2.3) in the momentum zone of the first Brillouin zone.

What is mostly of interests in graphene research is the behavior stemming from its electronic properties due to its particular electronic structure and the massless Dirac-fermion behavior [13-16].

The optical transitions of a graphene monolayer depend on its band structures. There are two types of particle optical excitations in graphene as shown in Figure 2.5. Figure 2.4 a depicts the interband transition whereby electrons absorbed photons and

are excited more into the conduction band. Since the speed of light is much larger than the Fermi velocity in graphene, such interband transitions connect two states with almost the same momentum. Apparently, because the position of the Fermi level is controlled by electrostatic gating, the threshold energy of interband transition can be continuously tuned. The interband transition mainly determined by the optical properties of graphene in infrared to visible and ultraviolet ranges.

The exciting fact about the interband transition in monolayer graphene is that, at zero temperature, the optical conductivity is determined by the fundamental constant as $\sigma_0 = \frac{\pi e^2}{2h}$, which is independent of frequency ω. As a result, the corresponding absorbance is $A(\omega) = \pi\alpha = 2.3\%$, where α is the fine structure constant. This frequency-independent universal optical conductance is not entirely unexpected since there is no characteristic energy scale in the linear band structure.

The other primary optical transition is the intraband transition as shown in Figure 2.4b. Such transitions connect the initial state and external state within the same band. Due to the significant mismatch between the speed of light and Fermi velocity, the intraband transition happens only with the momentum contributed by defects and impurities. The intraband transitions can be described by the tight binding model where the conductivity formulas are [20, 21].

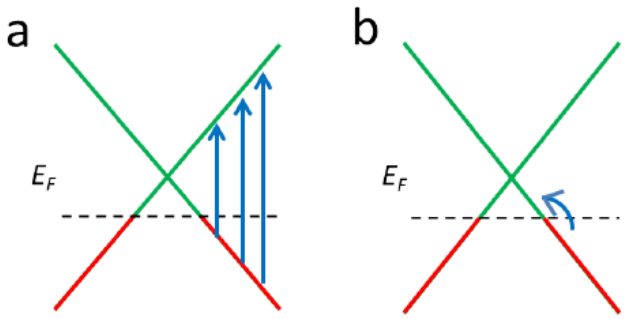

Figure 2.4 Optical transitions in monolayer graphene. a, Interband transitions from full state (red line) in the valence band to empty states (green line) in the conduction band. b, Intraband transitions from filled states to empty states in the same band.

The Figure 2.3 shows the energy dispersion of graphene near K points, this linear energy-momentum relation (equation (2-5)) enables graphene different from conventional semiconductors. Comparing this with massless particles obtained from Dirac equation, derived that the effective Fermi velocity of graphene is around $v_F \approx \frac{c}{300}$ [22].

The incredible electronic properties of graphene have greatly motivated the scientific community to pursue a better understanding of their primary physical features, with the hope of converting them into real technological applications. However, the lack of its electronic models restricts its applications on digital devices. Thus alternative strategies capable of inducing a band gap in graphene are being sought. Recently stacked graphene layers in the form of bilayers or graphite structures [23-25] have

offered a promising route for band gap manipulation.

2.2.2 Mechanical properties of graphene

Graphene has been confirmed as the "strongest material " based on its sustaining breaking strength of 42N/m with an intrinsic mechanical strain of ~25% and Young's modulus of Y~1.0Tpa [26]. Its automatic thickness can also be controlled by a mechanical stress measurement, which performed on graphene sheets subjected to deformation induced by depositing different insulating capping layers [27]. Various theoretical works have confirmed the experimental findings regarding to the main mechanical features of graphene. Among them, ab initio [28], tight binding [29], molecular dynamics simulations [30, 31], and semi-empirical models [32] have successfully estimated Young's modulus and other intrinsic mechanical quantities of graphene.

Figure 2.5 illustrates the toughness and strength of graphene and graphite versus the graphene sheet size in a theoretical research [33]. From Figure 2.5 a, we can see the c-bond graphene is stronger than graphite and h-bond graphene, the peaks for all three materials are reached when graphene sheet size around 25nm. For c-bond graphene, the toughness is between 300MPa to 400MPa, and the strength is about 14Gpa when graphene sheet size over 20nm. It proves suspended graphene is exceptionally resistant to mechanical force.

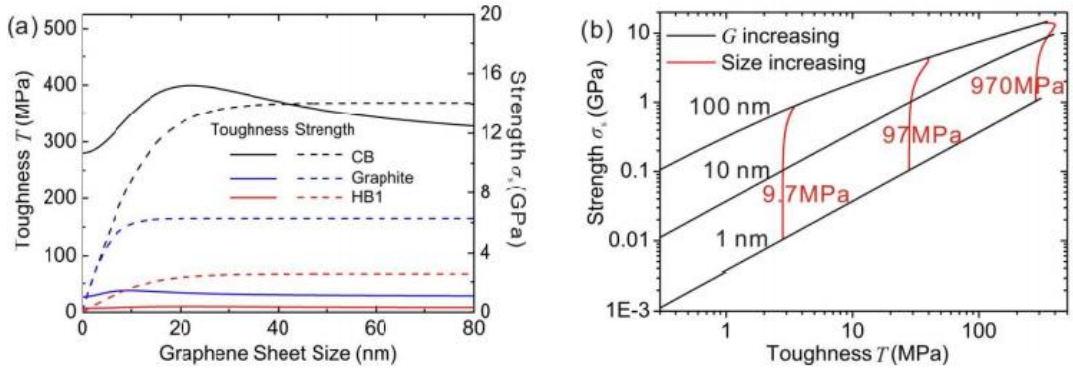

Figure 2.5 a. Plots of toughness and strength of coordinative bond graphene (CB), hydroxy1 graphene (HB1) and graphite; b. Tensile strength and toughness dependence on interlayer shear G and graphene size. [33]

2.2.3 Transport properties under external fields

The successful realization of graphene based nano-devices mostly depends on its unique electronic properties in thick atomic structure. In fact, when external fields like electric or magnetic fields and gate voltage under DC conditions worked on the low dimensional systems, some unique phenomenon can be observed. More importantly, the conductance of the system varies sharply by integer multiples of the quantum conductance concerning the strength of the electric field. Additional transport features

can be visualized when a rotating gate plate acts on the graphene ribbons. The transmission is shown to be dependent on the gate orientation and the width of ribbons [36]. External electric fields can also be used to efficiently tune critical physical quantities of graphene such as work function [37] and electron-phonon coupling [38].

An electric field effect (EFE) tuned electron-phonon coupling has been observed in Raman spectra of single-layer graphene [38] (shown in Figure 2.6). In the graph, the G band, the G-mode of Ramen spectra in graphene, depicts the in-plane vibration of carbon atoms in graphene. The G-band energy and the G-band width illustrate the energy normalization and the phone damping of graphene at G-mode respectively. G band is the gate voltage dependence of phonon frequency, and damping reveals charge-tunable interactions of optical phonons with Dirac fermion transitions across a vanishing band gap.

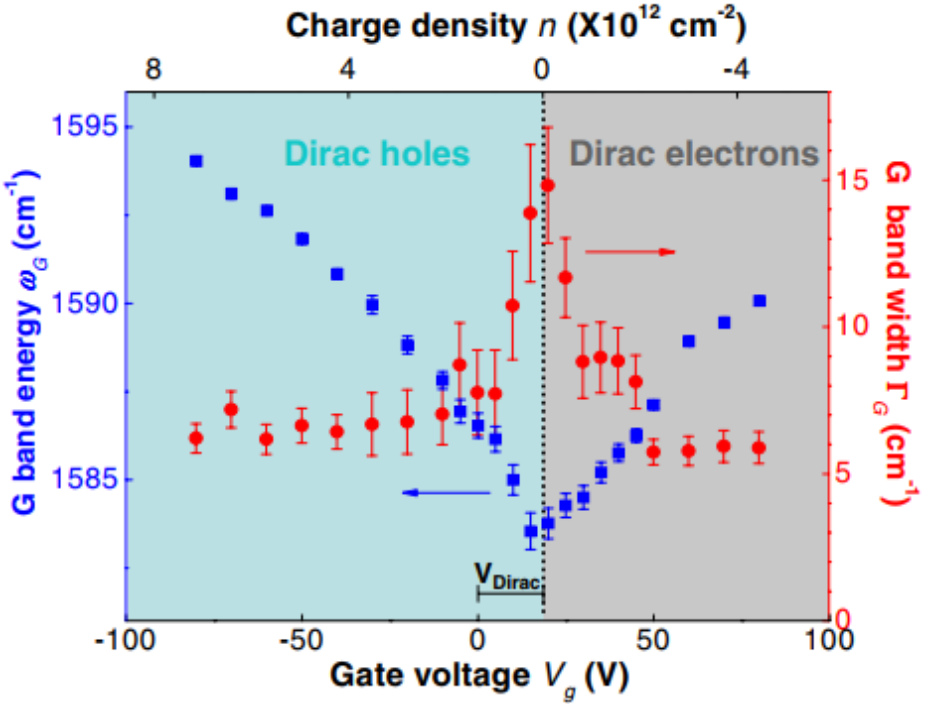

Figure 2.6 G band energy (squares) and G bandwidth (circles) of monolayer graphene under continuous gate voltage [38].

2.3 Optical properties of graphene

The electromagnetic properties of graphene are based on its unique atomic structure (see Figure 2.3) and the electronic band-gap between graphene sheet layers. As it is a two-dimensional material, the massless Dirac fermions in graphene have an amazing property: the optical response is universal and expressed only regarding to the fine-structure constant. To derive this response, we need determine the electric field of the incident light via a vector potential: $\vec{A}(t) = \vec{A}\exp(-i\omega t)$,

$$\vec{E}(t) = -\frac{1}{c}\frac{\partial \vec{A}}{\partial t} = \frac{i\omega}{c}\vec{A} \tag{2-7}$$

Thus, the incident working on the Hamiltonian of Dirac electrons in the presence of an electric field is [41]:

$$\hat{H} = v\vec{\sigma}\left(\hat{\vec{p}} - \frac{e}{c}\vec{A}\right) = \hat{H}_0 + \hat{H}_{int} \tag{2-8}$$

Where

$$\hat{H}_{int} = -\frac{ve}{2c}\vec{\sigma}\vec{A} = \frac{iev}{2\omega}\vec{\sigma}\vec{E} \tag{2-9}$$

is the Hamiltonian of the electron-photon interaction. The factor $\frac{1}{2}$ in equation (2-8) is necessary since the standard expression for the complex field is [41]:

$$\vec{E}(t) = Re\left[\vec{E}\exp(-i\omega t)\right] = \frac{1}{2}[\vec{E}\exp(-i\omega t) + \vec{E}^{*}\exp(i\omega t)] \tag{2-10}$$

And only the first term needs to take into account. This interaction induces transitions from the occupied hole states $\varphi_h(\vec{k})$ to empty electron states $\varphi_e(\vec{k})$ with the same wave vector $\vec{k}$, the intraband transitions being forbidden by the momentum conservation (Figure 2.4(a)). The matrix element of the Hamiltonian (equation (2-7)) is

$$\langle\varphi_h|\hat{H}_{int}|\varphi_e\rangle = \frac{ev}{2\omega}(E_y cos\phi \mp E_x sin\phi) \tag{2-11}$$

Where the negative and positive signs correspond to K and K` valleys. The sign depends only on the polar angle ϕ of the $\vec{k}$ vector, not on its length. After determining the average values, the square matrix element $|M|^2$ over ϕ is found [41]:

$$|M|^2 \equiv \overline{\left|\langle\varphi_h|\hat{H}_{int}|\varphi_e\rangle\right|^2} = \frac{e^2v^2}{8\omega^2}\left|\vec{E}\right|^2 \tag{2-12}$$

Here, assuming the photon propagates perpendicular to the graphene plane, thus, the electrical field $\vec{E} = (E_x, E_y, 0)$ lies within the plane. The absorption probability per unit time, to the lowest order of perturbation theory [39], is

$$P = \frac{2\pi}{\hbar}|M|^2 N\left(\mathcal{E} = \frac{\hbar\omega}{2}\right) \tag{2-13}$$

Where, $N(\mathcal{E}) = \frac{2|E|}{\pi\hbar^2 v^2}$ is the density of states (DOS) of single layer graphene (2D material DOS), the spin and valley degeneracy have been considered, and the energy of the final state is: $\frac{\hbar\omega}{2}$. Substituting the equation (2-12) and DOS expression into (2-13) results in:

$$P = \frac{e^2}{4\hbar^2\omega}\left|\vec{E}\right|^2 \tag{2-14}$$

Thus the absorption energy per unit time is

$$W_\alpha = P\hbar\omega = \frac{c}{4\hbar}\left|\vec{E}\right|^2 \tag{2-15}$$

Simultaneously, the incident energy flow is $W_i = \frac{c}{4\pi}\left|\vec{E}\right|^2$ [40]. Therefore the absorption coefficient is

$$A_0 = \frac{W_\alpha}{W_i} = \frac{\pi e^2}{\hbar c} = \frac{1}{137.04} \approx 2.3\% \tag{2-16}$$

This is a universal absorption for different frequency incidents on monolayer graphene. Moreover, it is much higher than the Fermi energy of electron hopping between layers of multilayer graphene or graphite. Therefore, the absorbance of N-layer graphene is NA_0 (shown in Figure 2.7). This behavior was observed experimentally for single layer and bilayer graphene [41].

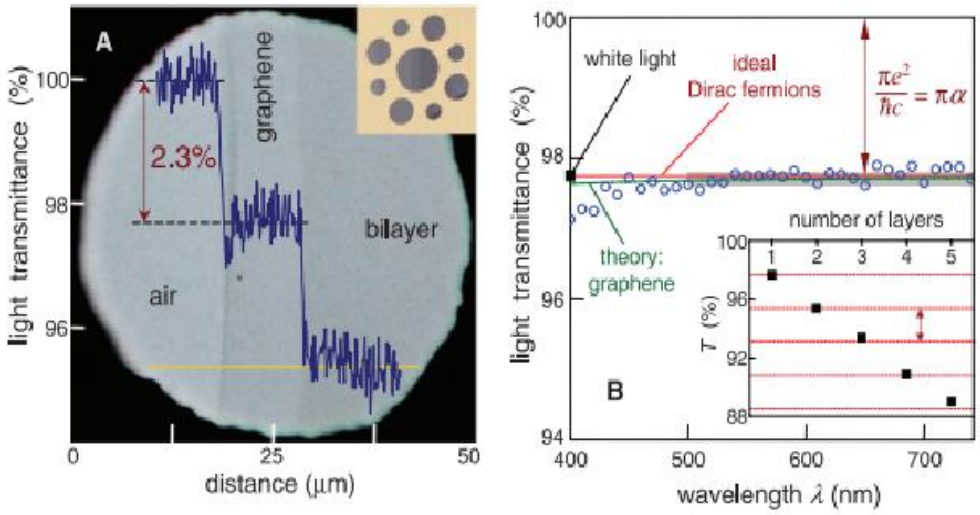

Figure 2.7 experimental results of absorbance of graphene under the 550nm incident. A. optical transmittance of monolayer and bilayer graphene; B. light transmittance tendency with different graphene layers [40]

The optical conductance of graphene defined from its linear dispersion relation, and can be expressed as:

$$\sigma = \sigma_r + i\sigma_i \tag{2-17}$$

Where σ_r and σ_i are the real and imaginary part respectively, which can be rewritten as [41]:

$$\sigma_r = \sigma_0\left[\frac{1}{2} + \frac{1}{72}\frac{(\hbar\omega)^2}{\xi^2}\right] \times \left(tanh\frac{\hbar\omega + 2\mu_c}{4k_BT} + tanh\frac{\hbar\omega - 2\mu_c}{4k_BT}\right) \tag{2-18}$$

$$\sigma_i = \sigma_0\left[\frac{\mu_c}{\hbar\omega}\frac{4}{\pi}\left(1 - \frac{2\mu_c^2}{9\xi^2}\right) - log\frac{|\hbar\omega + 2\mu_c|}{|\hbar\omega - 2\mu_c|}\left(\frac{1}{\pi} + \frac{1}{36\pi}\left(\frac{\hbar\omega}{\xi}\right)^2\right)\right] \tag{2-19}$$

Where $\xi \sim 3eV$ is the energy hopping between nearest atoms in the tight binding model [41], μ_c is the chemical potential near Dirac point, k_BT is the thermal energy, $\hbar\omega$ is the incident photon energy, and $\sigma_0 = \frac{\pi}{2}\cdot\frac{e^2}{h} \approx 6.08 \times 10^{-5}\Omega^{-1}$ is the universal graphene conductance. One theoretical work shows when the temperature T=300K

under visible incidents, the real part and imaginary part of graphene conductance are $\sigma_r = 1.016\sigma_0$ and $\sigma_i \sim 0$, respectively [42].

2.4 Optical refractive index of graphene

From Maxwell equations and Snell's law, displacement $\vec{D}$, magnetic field $\vec{H}$ and surface current $\vec{J}$ can be expressed as:

$$\vec{D} = \varepsilon_0 \vec{E} + \vec{P} = \varepsilon_0 \varepsilon_r \cdot \vec{E} \tag{2-20}$$

$$\vec{J} = \frac{\sigma}{d}\vec{E} \tag{2-21}$$

$$\nabla \times \vec{H} = \frac{\partial \vec{D}}{\partial t} = \vec{J} + \varepsilon_0 \frac{\partial \vec{E}}{\partial t} \tag{2-22}$$

Where $\vec{P}$ is the dielectric polarization, σ is the conductance, d is the material thickness. ε_0 is the free space permittivity ($8.854 \times 10^{-12} F/m$), and ε_r is the relative material permittivity, μ_0 is the open space magnetic permeability ($4\pi \times 10^{-7} H/m$), μ_r is relative permeability of the material.

Substitute equations (2-17) and (2-18) into (2-19), we can rewrite the equation as:

$$\frac{\sigma}{d}\vec{E} + i\omega\varepsilon_0\vec{E} = i\omega\varepsilon_0\varepsilon_r\vec{E} \tag{2-23}$$

We can extract the relative permittivity ε_r as:

$$\varepsilon_r = 1 + \frac{\sigma}{j\omega\varepsilon_0} \tag{2-24}$$

Definition of the refractive index of the medium is $n = \sqrt{\varepsilon_r \mu_r}$, which indicates the transmission efficiency in the medium. Regarding the linear susceptibility, the refractive index is $n_0 = \sqrt{\varepsilon_r}$, $\mu_r = 1$ when the material is graphene. Therefore, we can obtain the graphene refractive index as:

$$n_g = \sqrt{\varepsilon_r} = \sqrt{1 + \frac{\sigma}{j\omega\varepsilon_0}} \tag{2-25}$$

With the experimental discovery of isolated single-layer graphene in 2004 by Andre Geim and Konstantin Novoselov [1], came a flurry of research into its unique and exciting material and electronic properties. The typical optical response of graphene directly depends on its hexagonal lattice structure of carbon atoms, such as the universal absorption, the electrical conductivity and an easily tunable optical response. The linear energy dispersion relation of graphene sheet enables the surface plasmons propagation: charge density waves moving at the interface of graphene and electric materials. This excellent property supports graphene gating materials easily varying their plasmatic states broadly, making graphene a viable material for plasmonic applications from terahertz to mid-infrared frequencies. Gating structures involve two varieties, back-gating and top-gating. Both gates structures can provide the carrier

concentrations of graphene can be conveniently modified. With an applied voltage V, the adjusted carrier concentration N, in graphene is:

$$\mathrm{N} = \frac{\epsilon_{\mathrm{DC}} |\mathrm{V_G} - \mathrm{V_{CNP}}|}{\mathrm{ed}} \tag{2-26}$$

Where ϵ_{DC} is the dielectric constant of the gate dielectric, V_G is the voltage applied between graphene and the 1back-gate, V_{CNP} is the voltage of the charge neutrality point of graphene, e is the electron charge, and d is the thickness of the gate dielectric. The strength of the tuning, as well as the overall properties of graphene, are heaving dependent on its surrounding dielectric environment. As a result, it is essential to examine the range of dielectrics as substrates for graphene.

The research of tendency of graphene optical properties under manipulated external electric field, is an essential compliment to get better understanding for graphene. The graphene reflectance can be modulated by the applied gate voltage V on it. Therefore, the complex refractive index n can express as $n = n_0 + \delta n(V)$ in specific.

2.5 Optoelectronic application in graphene

Due to the unique properties of graphene, its applications in the optoelectronic field are from improving the performance and shrinking the size simultaneously for current devices.

Due to its excellent electronic properties, one promising application of graphene is the commercial scale electronic and photonic devices, such as graphene-based field-effect transistors (GFET) [44, 45], and THz optoelectronics devices [46].

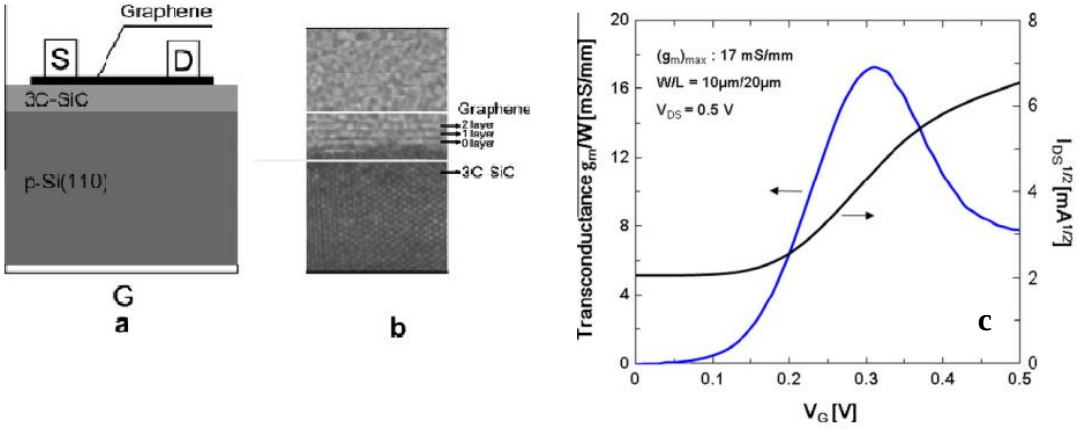

Figure 2.8 Back-gate graphene/Si FET fabrication and working efficiently. a. cross-section of GFETs; b. Fabricated section; c. Intrinsic transfer conductance with gate voltage [45]

A successful fabricated back gate GFET example and its characterization (Figure 2.8), which is monolayer graphene grown on 3C-SiC (80nm) layer (back-gate) [45]. This sample annealed under 1200 ℃, this relatively higher temperature decreases the gate leakage current. As shown observe in Figure 2.8c, the maximum trans-conductance of graphene/3C-SiC is 17mS/mm. The gate insulator thickness (80nm) with gate length of 20μm creates an impressive intrinsic transconductor 2.7S/mm.

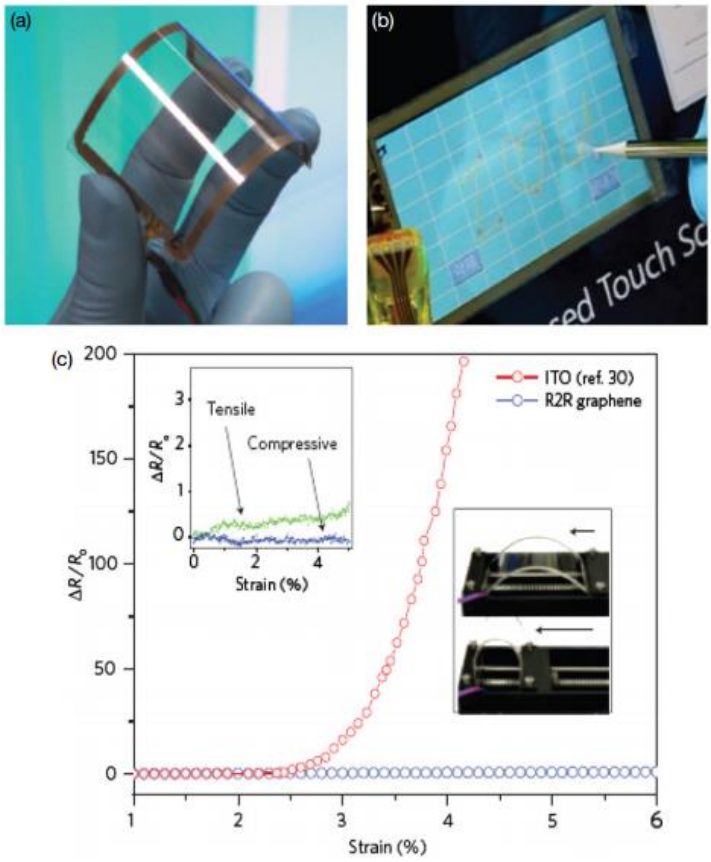

Figure 2.9 a. Excellent flexibility of an assembled graphene/PET touch panel; b. A graphene-based touch-screen panel connected to a computer with control software; c. Electro mechanical properties of graphene-based touch-screen devices compared with ITO/PET electrodes under tensile strain. [47].

A representative application of graphene-based film is the touchscreen, which already adapted to electrical devices, like cell phones and monitors. Fabrication of the graphene electrodes is etching oxygen plasma on monolayer, and then attaching the top and bottom films, shown in Figure 2.9.

Electrodes for optoelectronic devices, include liquid crystal displays (LCD) and organic light emitting diodes (OLED). Graphene is almost transparent ($T \cong 98\%$) to a wide range of light frequencies, which makes it be the perfect material to substitute for the current one (ITO). Graphene is also highly conductive, as we have previously mentioned and so it would work very well in optoelectronic applications such as LCD touchscreens, solar cell materials, and biosensors.

3 Graphene sample synthesizes

3.1 Introduction

In the last decade, due to its significance in both researches and applications, the need to produce high-quality large-scale graphene has stimulated many fabricating techniques. Among them, exfoliation [53-55] and thermal chemical vapor deposition (CVD) [56] are the popular ones. In the chapter, we introduce both synthesis methods and compare their advances and deficiencies. Also, we present the fabrication processes of graphene samples and graphene-based field effect transistors (GFETs) used our experiments.

3.2 Synthesis of graphene samples

The synthesis techniques of graphene includes two basic types, the top-down methods and bottom-up buildings (shown in Figure 3.1). The top-down fabrications means obtaining graphene from bulk materials such as graphite. Among these top-down methods, the mechanical exfoliation synthesis is the most financial reasonable and handful way to manufacture graphene, and this method first explored by Novoselov [9] in 2004. For the bottom-up techniques, most methods are basically growing graphene lyaers on different substrates. In 1970s, single atomic layer carbon structures fabricated on metal surfaces with thermal chemical vapor deposition (CVD) method [49-52].

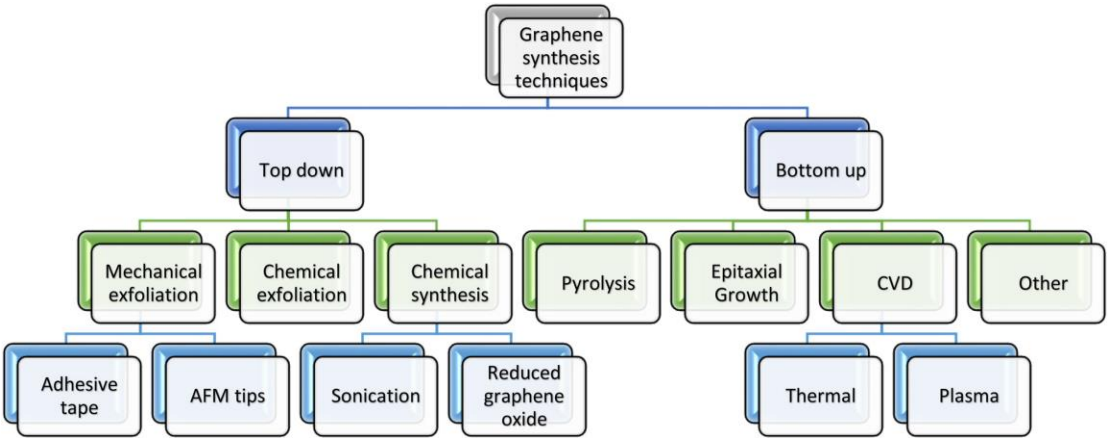

Figure 3.1 process of graphene synthesizes [51]

In those periods, their electronic properties never were investigated due to the difficulty in isolating and transferring them onto substrates. But after discovering of graphene in 2004 various techniques were developed to produce thin graphene films and few graphene layers. Due to its promising application, graphene synthesis has

encouraged various techniques developing. The most frequently used methods are exfoliation [53], chemical exfoliation [54, 55], and thermal chemical vapor deposition (CVD) [56].

3.2.1 Exfoliation of graphene

The first recognized method of graphene synthesis is mechanical exfoliation, which is a top-down technique in nanotechnology. The longitudinal separation of graphite can be created by the weaker van der Waals force between layers and much stronger chemical band force among atoms within same layer. A recent study demonstrates transfer printing of macroscopic graphene patterns from patterned HOPG using gold films [57]. It is by far the financially reasonable method to produce high-quality graphene. However, it is difficult to obtain high quality pure large-scale graphene with mechanical exfoliation method, not even taking into account the required layers of sustainable flakes. Figure 3.2 illustrates an application of graphene formed by mechanical exfoliation methods.

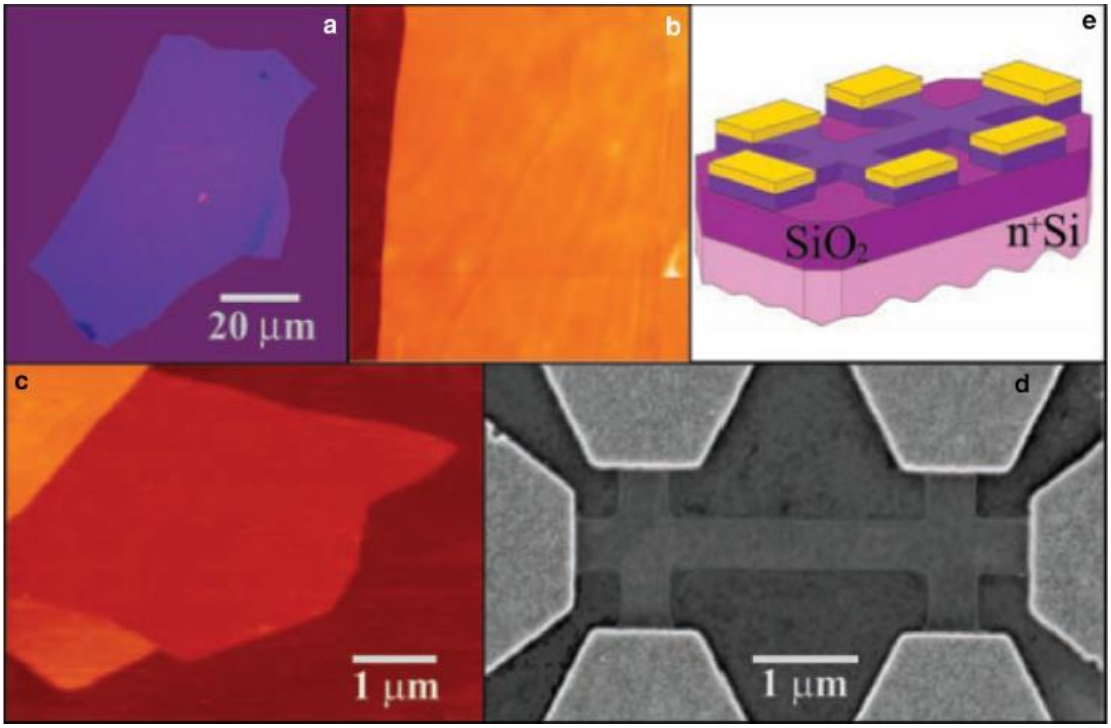

Figure 3.2 Graphene films. a Photograph (white light) of a large area multilayer graphene with $d = 3nm$ on top of SiO_2 wafer. b Atomic force microscope (AFM) image of the sample Size: 2mm ×2mm, SiO2 surface: dark brown; orange (3 nm height above the SiO2 surface). c AFM image of single-layer graphene. SiO2 substrate surface (dark brown); brown–red (0.8 nm height above the SiO2 surface); yellow-brown (1.2 nm higher); orange (2.5 nm higher). d Scanning electron microscope image for several-layer graphene. e Schematic view of the device design in (D) with permission of [58]

3.2.2 Chemical vapor deposition of graphene samples

Thermal chemical vapor deposition (CVD) is a chemical process by which a substrate exposed to thermally decomposed precursors and the desired product deposited onto the substrate surface at high temperature. Because the high temperature is nor desired in many cases, plasma-assisted decomposition and reaction may lower the process temperature. There are numerous advantages to the thermal CVD process. The process yields high quality and final purity products in large scale. Moreover, by controlling the CVD process parameters, control over the morphology, crystallinity, shape, and size of the desired outcome is possible. On the other hand, by applying a wide range of solid, liquid and gaseous precursor materials, a large variety of nanomaterial and thin films are executable with this process.

Deposition of mono-layer graphite material on Pt by thermal CVD first reported in 1975 by Lang *et al* [59]. They found that the decomposition of ethylene onto platinum results in the formation of a graphite over layer and surface rearrangements of the substrate. Later, Eizenberg and Blakely [60] reported graphite layer formation on Ni (111). The process involved the doping of single-crystal Ni (111) with carbon at an elevated temperature of 1200K-1300K for a significant period (~1 week), followed by quenching. The carbon phase condensation on Ni (111) was found with detailed thermodynamic analysis and the carbon phase segregation on Ni (111) is solely dependent upon the rate of quenching.

In 2006, the first attempt at graphene synthesis on Ni foil using CVD was made using camphor material [61]. In this reference, graphene synthesis was carried out in a two-step process, camphor deposition on TEM, they found that the planar few-layer graphene consists of ~35 layers of stacked single graphene sheets with an interlayer distance of 0.34nm. The study presents a new path toward large-scale graphene growth using thermal CVD. Nevertheless, widespread monolayer or bilayer graphene growth with thermal CVD was still in demand until Obraztsov *et al* [62] reported the deposition of thin-layer graphite on Ni. Figure 3.3 shows the thickness of final graphene on Ni was ~1-2nm covered with surface ridges, which explained thermal expansion coefficient mismatch between graphene and the Ni substrate. Also, from the Figure 3.3, we can see the well-ordered few-layer graphene was found on the Ni surface (in Figure 3.3 b and c), but not existed on Si substrate (in a) except amorphous carbon.

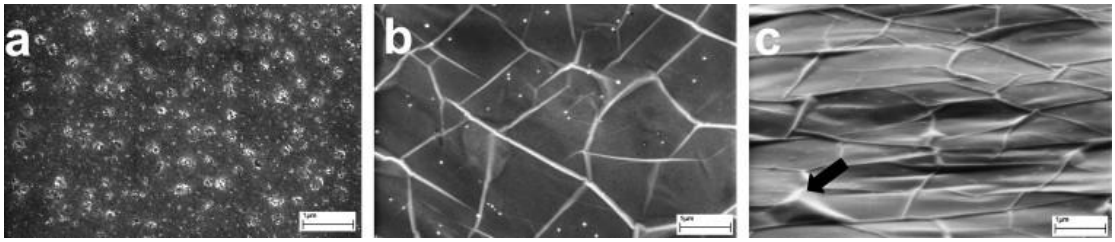

Figure 3.3 scanning electron micrograph of graphene synthesis on Si (a) and Ni (111) (b, c) by DC discharge method. [60]

A breakthrough occurred in the field of large-scale graphene synthesis process when Cu foil (15cm × 5cm) was rolled up and place in quartz tube furnace to grow graphene and then transfer the graphene flake onto polymer materials substrate using the hot press lamination method. The Choi group [63] reported a large-area graphene growth as massive as a 15cm × 5cm rectangular Cu foil using the thermal CVD technique. Graphene deposited at 1000℃ with a mixture of H_2: CH_4 (1:4) at ambient atmospheric pressure, and then graphene was transferred using a hot press lamination process (shown in Figure 3.4), which was proficient as well as industrially scalable. Their work demonstrated large area graphene on flexible film can be used as a current collector in a flexible transparent field emission device.

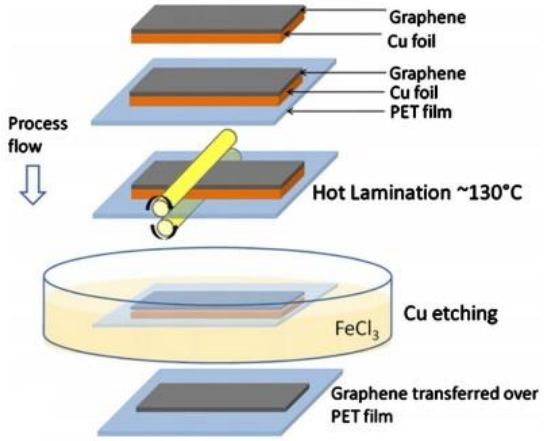

Figure 3.4 The hot pressure lamination process for graphene-PET film fabrication [63]

The graphene/SiO_2/Si samples we used in reflection experiments were grown on thin commercial copper foils at 1000℃ in a CVD system using a similar procedure in reference [64]. The Cu foil was heated in a mixture of H_2: CH_4 (1:5) to initiate the graphene growth under around 500mTorr ambient pressure. Graphene precipitation on dielectric surfaces occurred due to the surface catalyzed process of Cu and the copper films de-wetted and evaporated from the surface, which leads to direct graphene deposition on SiO_2/Si substrate (Figure 3.5 shows the samples photograph). The samples were fabricated by external company.

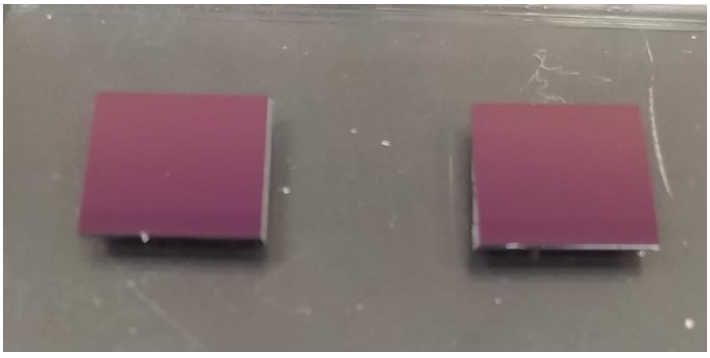

Figure 3.5 Photograph of Graphene/SiO_2/Si samples in experiments with single-layer graphene on top of SiO_2 with 300nm thickness and Si (525μm) and back side etched the size of

sample is 8mm ×8mm

3.2.3 Preparation of gated graphene

The graphene gating structures involves two types: top-gating and back-gating, and both structures can work as the generally electronic and photonic devices. According to the experimental results [64-69], the top-gate materials applied more as graphene based field effect transistors, the back-gate samples more used as optical sensors. Synthesizes of two types are similar, and the most frequent method is CVD. Now the graphene based optoelectronic devices have already been able to tune the local carrier concentrations and conductance. And it has already fulfilled on supported samples both with the bottom and top gates [64-67].

The fabrication of back-gating graphene includes three steps. First, obtain graphene flakes through exfoliation or CVD methods; then the graphene layers has been transferred onto the dielectric material (substrate) and characterized under scanning techniques (such as atomic force microscopy or Raman spectroscopy). After characterization, add the back-gate on the other surface of the substrate, the back gate materials are usually metals (*Ti* and *Ni*).

In this study, we use top-gate graphene samples in our experiments. We implemented graphene-based field effect transistors (GFET) to explore the optical properties changing when they work as a nano-scale GFET device. Regarding to the isolated graphene, the fabrication of local top gates are still challenging due to the uncertainty of ions doping during the procedure, which has been reported in the community [68-70].

Figure 3.6 describes the structure design of local gates (GFET). To do so, we chose a dry transfer technique [71]. At beginning, graphene was grown on Cu foil with thermal CVD method, and transferred onto a separate wafer of SiO_2/Si with a stack of PMMA of 5nm/300 nm. And then grown the source and drain terminals at the holes without PMMA, and no specific resists stack need for this step. Afterward, a thin Al_2O_3 film with the gain structure on the top surface, has been place on the top of source and drain surface. At last, placed the wafer piece at the surface of DI-water, and the PMMA layer slowly dissolved [71]. Then the glass slide is transferred to a modified Al_2O_3 mask aligner to realize the alignment between the graphene flake and the top-gating.

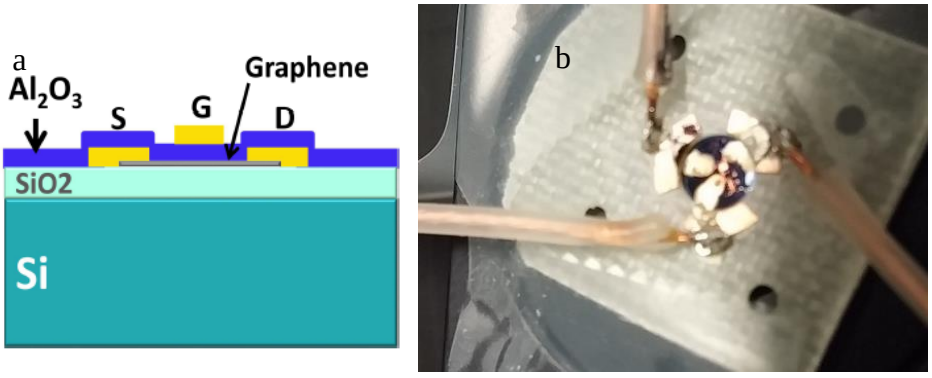

Figure 3.6 (a) The schematic of top-gate graphene after gate structure. (b) The sample after

fabrication

Figure 3.6b depicts the design of the graphene-based local field effect transistor, the entire top gating chip structure is source and gate terminal formed voltage bias and drain end connects to ground. The photocurrent between source and drain will be generated when a beam propagates on the graphene FETs. Figure 3.7a) illustrates the full device structure and the connection between small FET biases, there is 6×6 micro junction on the whole chip. The microstructure of single FET bias shown in Figure 3.7 (b), the left end of the intersection is source terminal and the fork formed structure at the right end is gate terminal. The full size of the top gating chip is 50 μm×50 μm. And the fabrication of the chip is done in the QNC ultraclean lab.

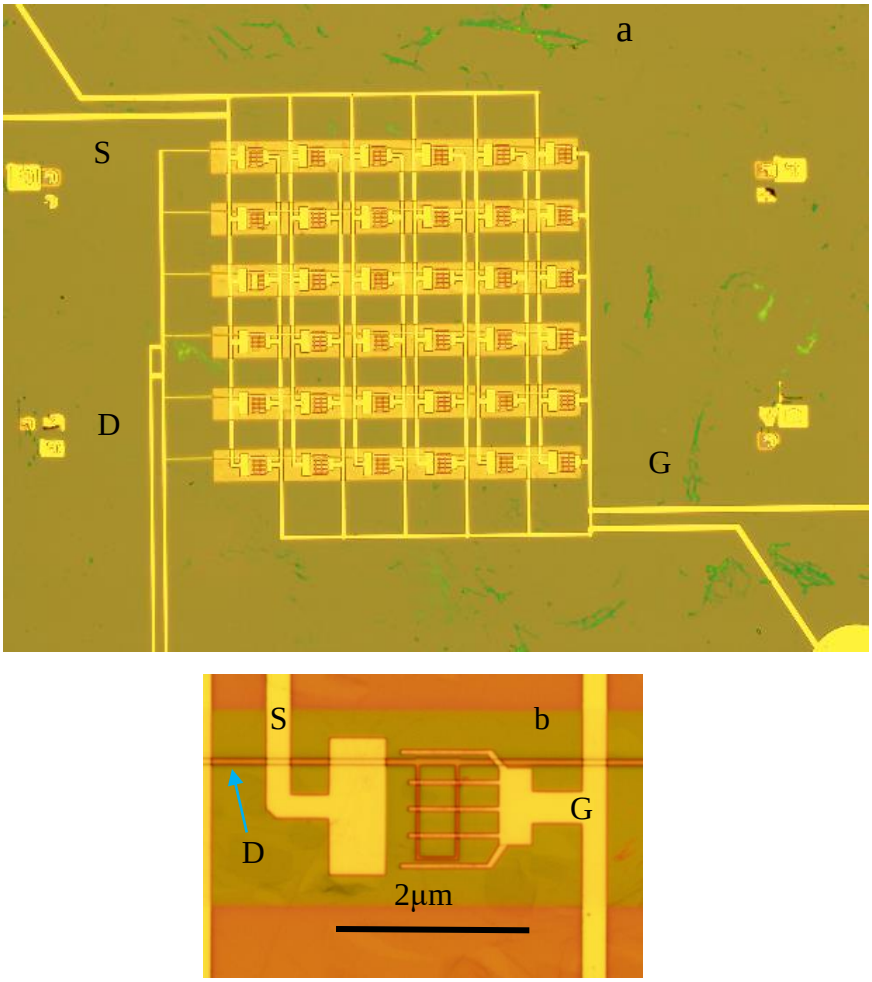

Figure 3.7 GFET design structure (a) full gating chip schematic the two left terminals are Source and Drain the right terminal is top-gating. (b) Microstructure of single GFET

We can see (Figure 3.7 a) the entire GFET chip composed by a 6×6 array of micro graphene-based field effect transistors (each size of 2μm). This structure can enlarge the efficient contact between graphene atoms and source and drain parts, which provides the GFET more sensitive to the incident beam. The specific microstructure of

GFET is shown in Figure 3.7 b. The gate side shaping as a fork, this unique structure is similar to the resonator, which can enhance the signals it received.

3.3 Conclusion

In this section, we introduced two most frequently used methods for graphene fabrication, exfoliation and thermal CVD, and commented both ways, and derived thermal CVD is the more applicable technique to produce large-scale and pure desired graphene layers. Then we gave the fabrication process of our experimental samples. The samples for reflection tests were grown on copper foil and then transferred onto the Si/SiO_2 substrate with CVD technique. The gated sample was fabricated on the top of the former graphene/Si/SiO_2, the first source and drain sides grown and then the gate with CVD procedure.

In our experiments, we use optical reflection and transmission method to obtain the optical constants value. In next chapter we will discuss the tests and results in detail, which is the experimental part.

4 Graphene refractive index experiments

In this chapter, we focus on reflection measurements of different graphene samples response to infrared lasers to obtain RI of graphene. There are three parts in this chapter; the first subsection depicts the reflection system design. The second part is the reflection tests of graphene samples, begins with the setup built, Gaussian beam characterizations, and the results discussions. The last section illustrates gated graphene samples reflection probe and complex refractive index tunability discussion.

4.1 Optical reflection setup design

To determine the complex refractive index of graphene generally through measure the optical reflection and transmission of graphene samples. And there are following methods to do the test, such as surface plasmon resonance (SPR) angle detection [72][73], Spectroscopic ellipsometry [74][75], and reflection spectroscopy [76]. Because of complex RI has two unknown variables, any single set of measurements can only provide one constraint. Therefore, the optical methods for testing the linear response of graphene samples in this thesis are reflection spectroscopy and tunability of optical reflection via external voltage. This section will introduce the reflection setup design in our work.

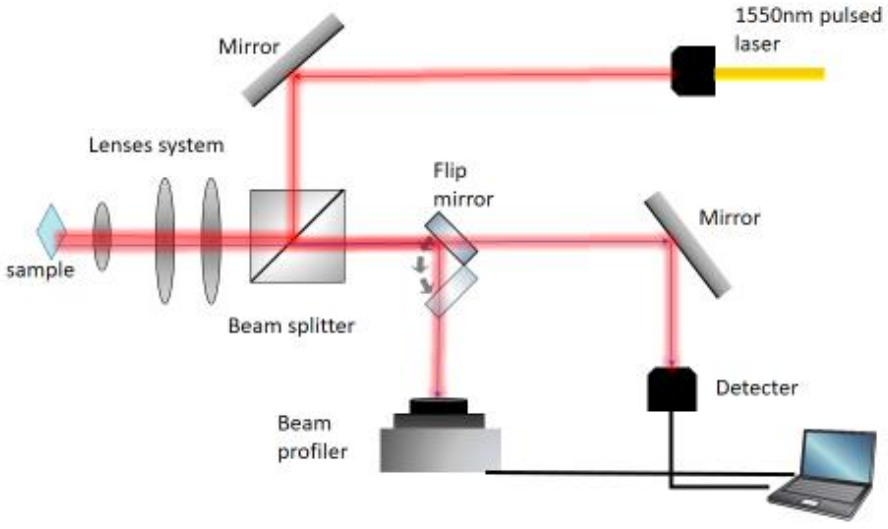

Figure 4.1 Sketch of optical spectroscopy setup. From the sketch, the laser beam comes from the fiber laser diode, through a collimator and a mirror to adjust direction of the incident; and passes a 50:50 beam splitter and focus on the sample. Reflection beam begins from sample and through the focal system, beam splitter, and a flip mirror and detected by the beam profiler, and when the beam spot size at the waist, turn the flip mirror off to make the beam collected by the

power detector.

The setup of optical reflection test (Figure 4.1) applied to making graphene samples to illuminate strong intensity of incidents, which from pigtail diode laser (wavelength is 1550nm). Then the beam is reflected twice by a metallic mirror and a 50:50 cubic beam splitter, which used to adjust the beam propagate direction and guarantee the incident is perpendicular to the sample surface. After the angle correct, the light passed through a designed focal system (section 4.1.1) and focus on graphene sample (shown in Figure 4.1).

The reflection beam was generated on the sample, and the path overlapped with the incident during the focal system, and then passed through the beam splitter. Afterward, the reflective light detected by a beam profiler, which checks the beam shape. At last, the reflected signal was collected into the detector of power meter.

4.1.1 Focal lenses system design

In the whole setup, from former chapter the size of samples is relatively minimum, usually $50\,\mu m$ to $100\,\mu m$, which requires the focal system is a significant precise, to obtain the smallest focus spot on the sample. We designed an infrared focal system with three focal lenses.

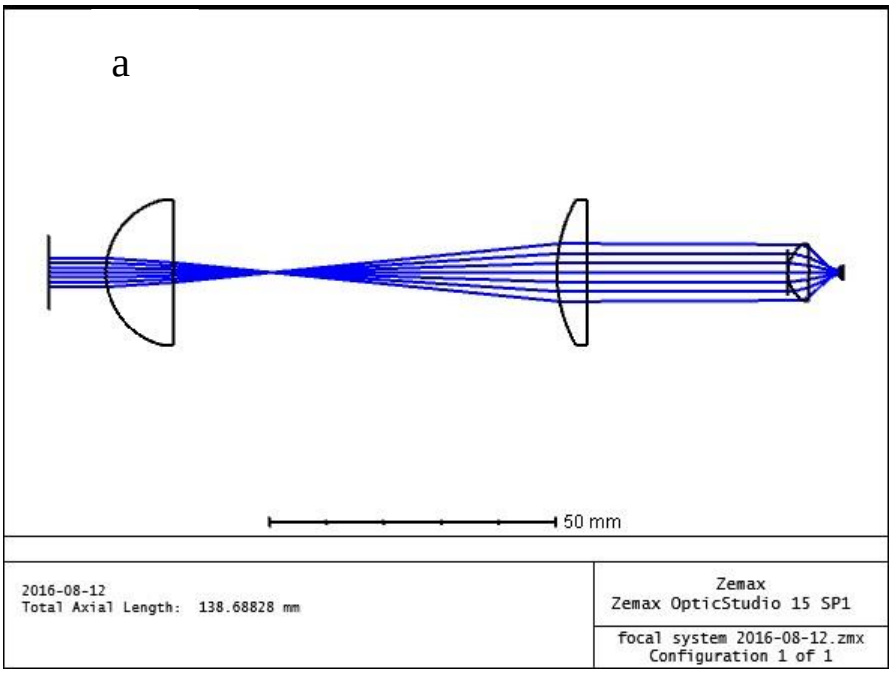

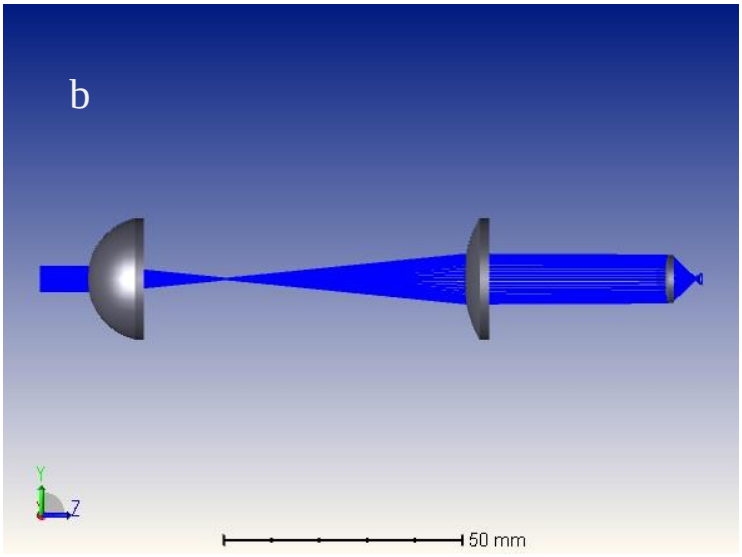

Figure 4.2 The review of the focal system. a) Depicts the whole sketch of the lenses and the distances between different lenses. b) The light intensity and focus capability.

From the above figures, the light comes from the left side; the two larger plano-convex lenses are used to spread the beam and create the collimated beam, if the incident light is not perfect collimated, and the third small lens is a gel-tech focal lens the focus spot can reach $5\mu m$. An optical designing software "Zemax" was applied to design the entire focal system, and the simulation of light propagates the system from the left side is depicted in Figure 4.2.

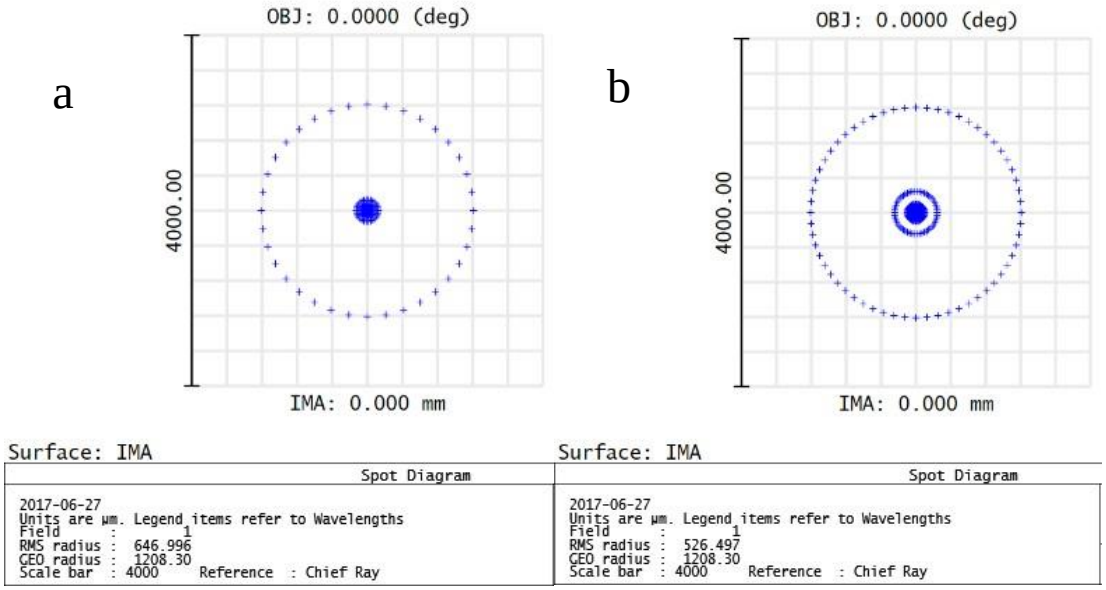

Figure 4.3 The beam spot sizes of the focal system. a) Beam spot at focal point spot radius is $20\mu m$; b) beam spot at the position to focal point 5 μm, the spot radius is 55 μm.

This focal lenses system is designed for infrared light and provide a perfect small focal point on samples, allowing precision alignment with negligible power loss. The

performance of this design operates quite well (shown in Figure 4.3) in our experiments, it enables the beam illuminating on the graphene area without transmittance loss.

4.1.2 Gaussian beam construction

The incident beams in our experiments are laser beam (Gaussian beam), to dispose of data conveniently, we construct the individual Gaussian beam. Starting from a *z*-axis propagating beam with the electric field $\vec{E}$ and the wave vector $\vec{k} = (k_x, k_y, k_z)$ leaving the *x* and *y* directions to describe the transverse part of the beam[77]:

$$\frac{\partial^2 \vec{E}}{\partial x^2} + \frac{\partial^2 \vec{E}}{\partial y^2} + 2ik\frac{\partial \vec{E}}{\partial z} = 0 \tag{4-1}$$

Figure 4.4 is the sketch of parameters of a Gaussian beam.

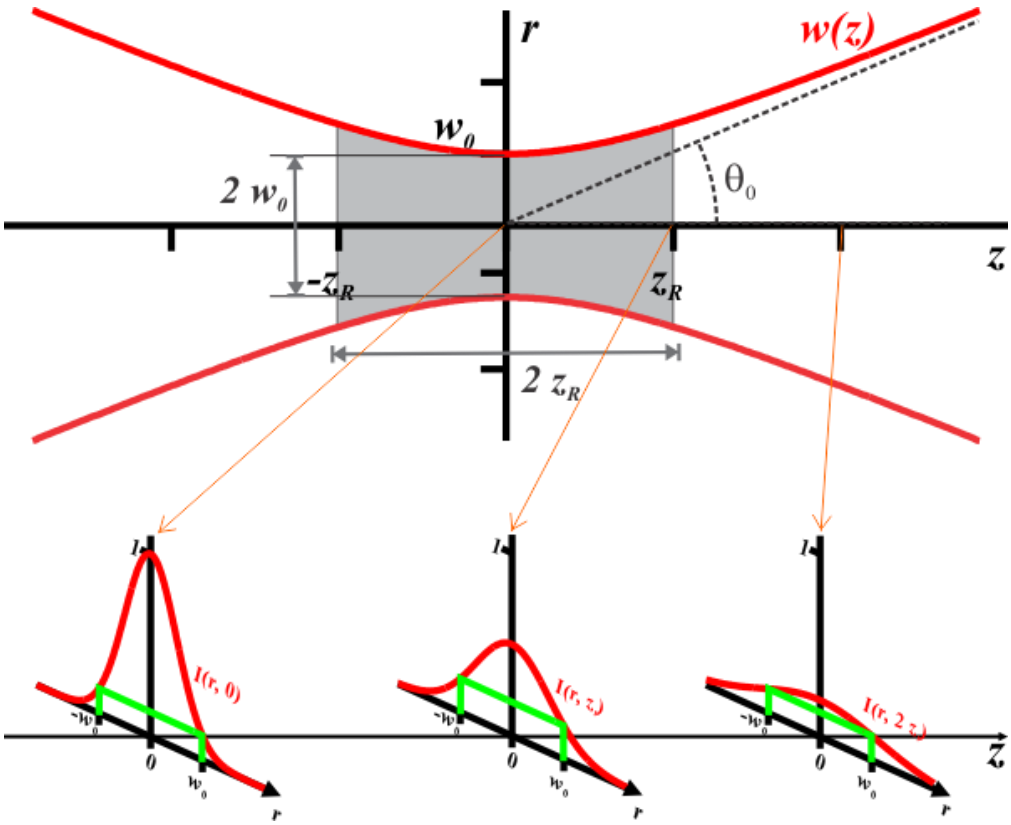

Figure 4.4 Gaussian beam as function of distance *z* along the beam

Leads to the Gaussian beam equation (showed in Fig 4.4):

$$\vec{\mathrm{E}}(\mathrm{x},\mathrm{y},\mathrm{z},\mathrm{t}) = \vec{\mathrm{A}}\frac{\omega_0}{\omega(z)} e^{-\frac{x^2+y^2}{\omega(z)^2}} e^{i(kz-\omega t)} e^{\frac{ik(x^2+y^2)}{2R(z)}} e^{-i\phi(z)} \tag{4-2}$$

In this transformation, ω_0 is the beam-waist;

$\omega(z)$ represents the beam spot width, and its value increases along with the z-axis direction;

R(z) illustrates the beam divergence called the radius of the wavefront curvature, which is given by $\mathrm{R(z)} = \mathrm{z} + \frac{z_R^2}{z}$;

z_R is a constant called Raleigh range, determined by beam waist ω_0 and incident wavelength λ: $z_R = \frac{\pi\omega_0}{\lambda}$;

$\phi(z)$ is the Gouy phase of the beam at position z is given by $\phi(z) = \arctan(\frac{z}{z_R})$.

Construct the incident laser beam, Gaussian beam with M^2 methodology (beam quality factor), which is propagation ratio that indicates how close a laser is to be a single mode TEM_{00} condition the M^2=1.

For a laser beam propagation through lens, the equation of the divergence angle θ_0 is given by

$$\theta_0 = M^2 \cdot 4\lambda/\pi D \tag{4-3}$$

Figure 4.5 depicts the test results for Gaussian beam shaping

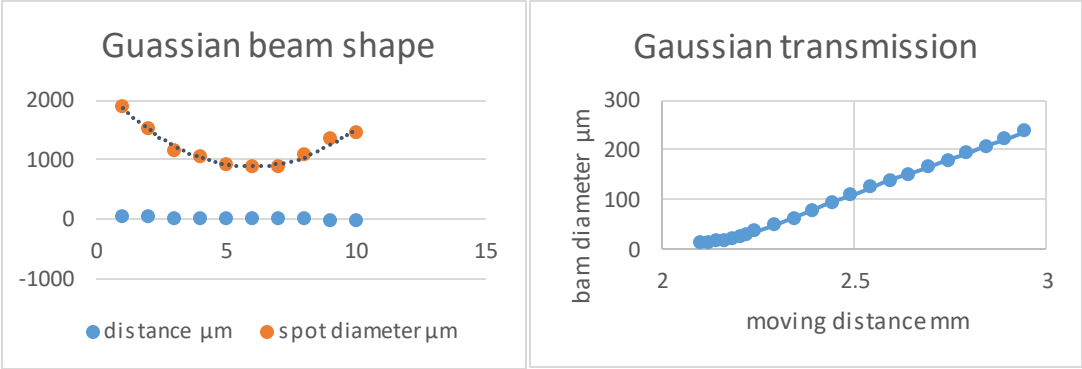

Figure 4.5 Experiment results of Gaussian beam shape

Measure the Rayleigh range of the Gaussian beam from the experimental results.

From the beam diameter of Gaussian beam at different distances around the waist, can derive the Rayleigh range of incident beam.

$$Z_R = \frac{\pi\omega_0^2}{\lambda} = 456.03\mu m \tag{4-4}$$

Where ω_0 and λ are the beam waist and wavelength of the incident, respectively.

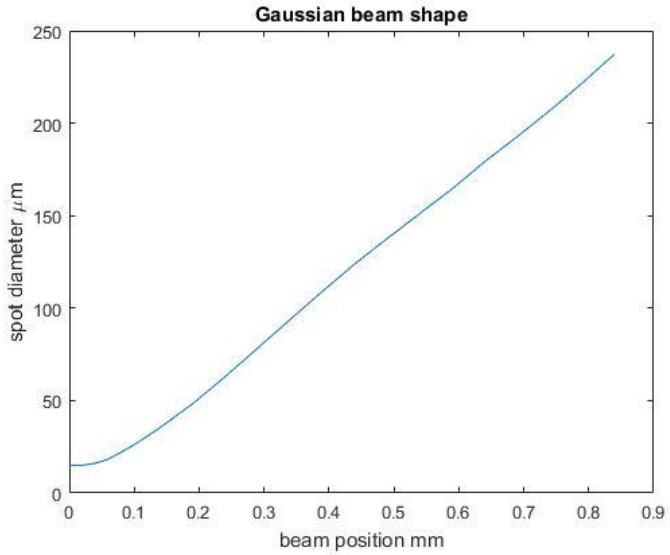

Figure 4.6 Incident Gaussian beam shape

Then, the spot size of the full width (FWHM) at half maximum beam is:

$$\omega(z) = \frac{FWHM(z)}{\sqrt{2ln2}} = 170\mu m \tag{4-5}$$

The curvature of the wave-fronts is:

$$R(z) = z\left[1 + \left(\frac{Z_R}{z}\right)^2\right] = \frac{z^2 + Z_R^2}{z}. \tag{4-6}$$

The parameters of the construction of incident Gaussian beam are derived, so can obtain the wave function of the Gaussian beam of incident wave in experiments (showed in Table 4-1):

Table 4-1 Parameters of Gaussian beam in experiments

parameters	value	unit	meaning
$\boldsymbol{\omega_0}$	$2\pi/1.55$	10^6	Incident frequency
$\boldsymbol{\omega(z)}$	$2\pi/170$	10^6	FWHM of beam spot
R(z)	465	μm	Radius of wave-front curvature

According to the simulation of graphene sample reflection, the incidents of the beams are plane waves. But in experiments, the incidents are laser beams (Gaussian beams. Therefore, need to expand the Gaussian beam into plane waves. Put Gaussian beam as the summation of TE mode and TM modes. One theoretical research derived the power changes when the beam incident on graphene material with an angle θ_i [78], shown in Figure 4.7. But this influence is minimum in our case (the reflective power decreases about 5% in both modes), since the incident is perpendicular to the surface of the sample.

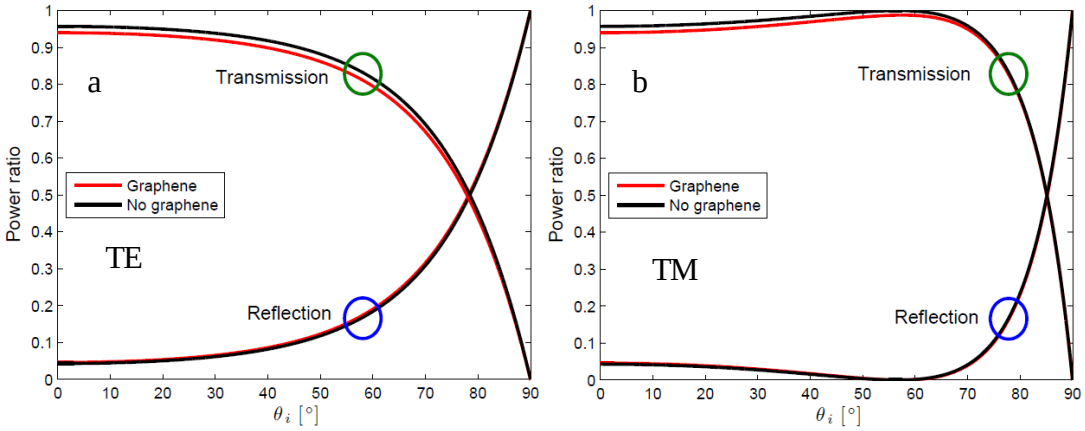

Figure 4.7 The reflection and transmission ratios versus plane wave incident angle on graphene soda-lime. a. TE mode; b. TM mode [78]

4.2 Optical reflection on graphene samples

4.2.1 Setup introduction

The linear optical response of graphene first attracted attention for its significance in quantitative identification of different graphene layers through optical reflection on oxidized silicon substrates [79]. This demonstration allowed the possibility of private single atomic planes of graphite on an insulating substrate and fabrication of electrical devices. It was immediately realized that optical contrast of graphene is a key feature for its application. The standard thin films optics approach is based on predicting the contrast of graphene flakes deposited on various substrates in different spectral range like terahertz [80], visible [81], infrared [82]. Most of the researches focus on visible range, bare papers on the infrared range. Although the researches are in agreement with a universal conductance theory, there remains a disparate set of reported refractive index values for graphene (Table 4-2).

Table 4-2 Comparisons between synthesizes of Graphene RI

Reference	**Method**	**λ**	**(n_g, k_g)**	**sample**	**substrate**
Ni *et al.* (2007)[83]	Reflection spectroscopy,	White light	(2.0, 1.2)	Exfoliation 1L	SiO_2
Bruna & Borini (2009)[76]	Reflection	550nm	(3.0, 1.15)	Exfoliation 1L~2L	Si/SiO_2
Matkovic *et al* (2012)[84]	Spectroscopic ellipsometry	500nm	(2.7, 1.45)	Exfoliation 1L	Si/SiO_2

Ye *et al* (2013)[85]	SPR in air	532nm	(2.6, 1.6)	CVD 1L~2L	Polydimethylsiloxane (1mm)
Xue *et al* (2013)[86]	SPR: in water	500nm	(2.75, 0.41)	GO 1L	Plasmon resonance
Klintenberg *et al* (2012)[87]	Amplitude and phase change of reflected light when a focused monochromatic light traverses a graphene boundary.	550nm	(2.96, 1.49)	Exfoliation 1L	SiC
E. D. Palik [88]	Optical Reflection	515nm	2.675, 1.35	Graphite crystal	
G. E. Jellison *et al* [89]	Ellipsometry	450nm-750nm	2.52, 1.94	Graphite crystal	
R. Ahuja *et al* [90]	Full band theory	532nm	3.0, 1.38		
X. Wang *et al* [91]	picometrology	532nm	2.4, 1.15	SiO_2 (285nm)	SiO_2 (285nm)
M. Klintenberg *et al* [100]	Full band theory	visible	2.79, 1.48	1L graphene	
Current work	Optical Reflection	1550nm	2.75, 1.57	1L graphene	SiO_2 (300nm) Si (525μm)

From the table 4-2, we can see that all the experimental results are in visible range, but the values do not quite agree with each other.

In this section, we show a systematical measurement of refractive index by optical reflection spectroscopy on monolayer graphene. The whole setup depicted in Figure 4.1 (sketch) and Figure 4.8 (photograph).

To determine the linear reflection coefficient of graphene, first, the reflection power ratio of monolayer graphene on top of the SiO_2/Si substrate was measured; for this, the experimental setup is depicted in Figure 4.1. The excitation source is a quantum well laser diode, where the beam goes through a beam-splitter and focal lens system, focusing on the sample. Then the reflection signal is monitored by a beam profiler and collected by the detector. This latter connects to the power meter.

This test using 1550nm pulse laser as incident and measured the reflection power

from mirror and graphene samples respectively. The reflection from the mirror is the reference of power ratio.

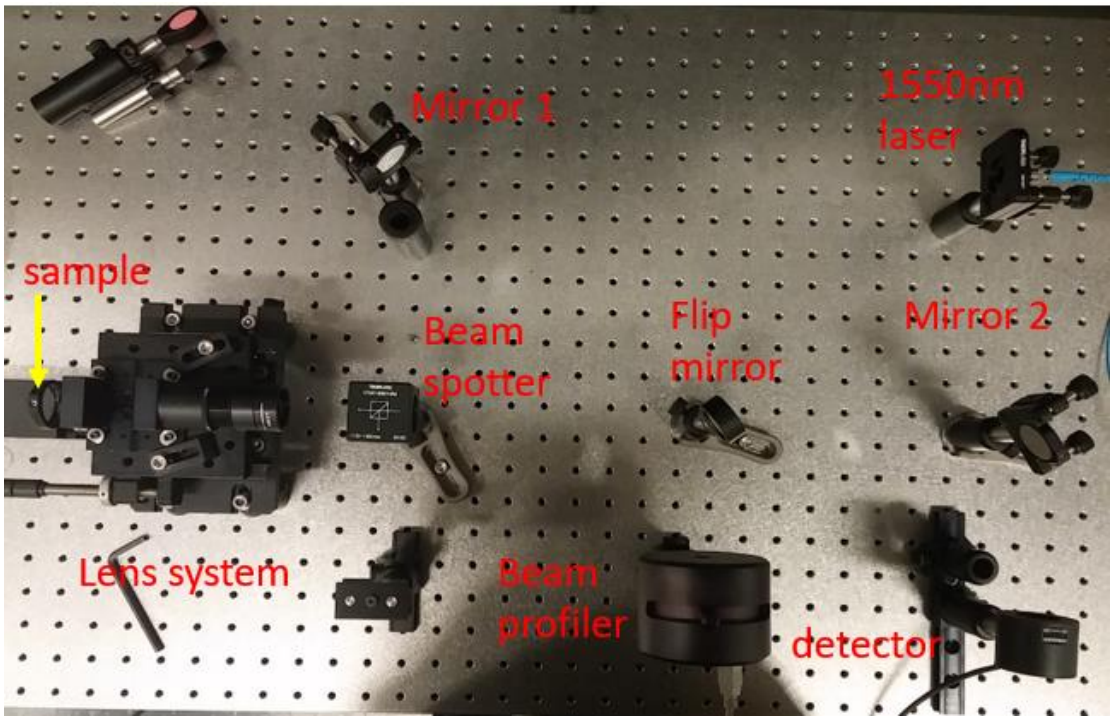

Figure 4.8 Photograph of reflection experiment setup

The components in the setup (Figure 4.8) are:

Incident source: 1550nm pigtail fibre laser;

Collimating lens: 1550nm optical fibre-free space collimator;

Reflector 1 for incident: silver metallic mirror;

Reflector 2 for incident: 50:50 infrared beam splitter, available wavelength range 900nm-1600nm;

Focal system: (from right to left in Figure 4.8)

1. Plano-convex lens with 1050nm-1600nm coating, size: 1inch, focal length:35mm;
2. Plano-convex lens with 1150nm-1950nm coating, size: 1inch, focal length: 75mm;
3. Plano-convex gel-tech lens with 1050nm-1600nm coating, size: 12mm, focal length: 4.9mm.

Reflector 3: Flip metallic mirror;

Beam waist probe: infrared beam profiler, enable wavelength range 900nm-1600nm;

Reflector 4: metallic mirror;

Power detector: detector of a power meter.

Samples used are differently prepared monolayer graphene on top of SiO_2 thickness 300nm$\pm$5nm and Si thickness 525μm (shown in Figure 4.9). The experiment process is collecting the reflections power around the Gaussian beam waist from the reference mirror and the samples respectively.

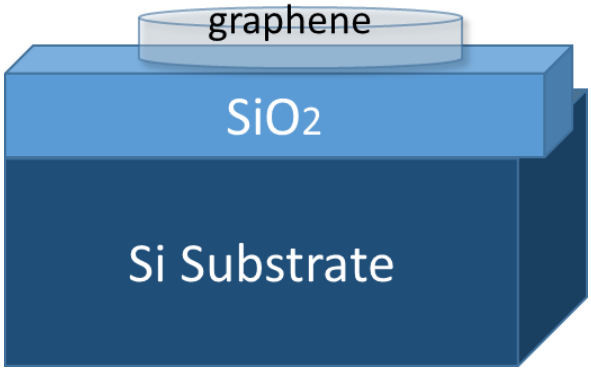

Figure 4.9 Objective of graphene sample

4.2.2 Calculation method of graphene refractive index

The optical reflection and transmission of N-layers medium calculation is based on Snell's law, Maxwell equations and their boundary conditions. In our case, it is a 5-layer medium (air, graphene, SiO_2, Si, and air), with different thickness at each layer. Due to the energy loss mechanisms [102] in such samples a depth profile occurs for the change of the optical constants (n_g in our samples). The calculation of reflectance and transmittance of the 5-layer medium (Figure 4.9), are as a function of the wavelength λ, the multilayer system with thicknesses d_i, and different optical constants n_i. Restricting to the usual experimental conditions a perpendicular incidence is taken into consideration.

Because of the linearity of Maxwell equations the reflection and the transmission of the light from the front and the back side of a plane-parallel system may be described uniquely by transfer matrix equation:

$$\bar{M} = \bar{M}_{4,5} * \cdots * \bar{M}_{1,2}\bar{M}_{0,1}$$

As the complex reflection and transmission coefficients for the incoming waves propagating in $\pm\hat{z}$ directions at the surface between the (*m-1*)-th and *m*-the layer. There is a simple relation between the phase ϕ_m and the thickness d_m, refractive index n_m for the lossless medium. However, the multilayer medium is lossy in our experiments, which means the refractive index n_m should change to $n_m = n'_m - ik_m$. Therefore, the transfer matrices convert to [105]

$$\bar{M}_{m-1,m} = \begin{bmatrix} e^{-j\phi_{m-1}}\left(1+\frac{k_z^{m-1}n_m^2}{k_z^k n_{k-1}^2}\right) & e^{-j\phi_{m-1}}\left(1+\frac{k_z^{m-1}n_m^2}{k_z^{k-1}n_k^2}\right) \\ e^{-j\phi_{m-1}}\left(1+\frac{k_z^{m-1}n_k^2}{k_z^{m-1}n_{m-1}^2}\right) & e^{-j\phi_{m-1}}\left(1+\frac{k_z^{m-1}n_k^2}{k_z^{m-1}n_m^2}\right) \end{bmatrix} \quad (4\text{-}7)$$

Where phase ϕ_{m-1} is defined as $\phi_m = k_z^{(m)}x_m$, in which x_m is the propagating position of the incident at the interface of two layers. And the longitudinal wave number can be obtained as [103].

$$k_z^{(m)} = \sqrt{n_m^2 k_0^2 - |k_t|^2}, \quad Im\{k_z^k\} < 0 \tag{4-8}$$

The reflection coefficient is:

$$r = \left[\frac{(M_{21} + k_l k_R M_{12}) + i(k_l M_{22} - k_R M_{11})}{(-M_{21} + k_l k_R M_{12}) + i(k_l M_{22} + k_R M_{11})}\right] \tag{4-9}$$

Derive the reflectivity:

$$R = |r|^2 \tag{4-10}$$

The measured ratios of the light intensities can be calculated by the absolute square of the amplitude ratios taking into account the Poynting vector is proportional to the square of the electric field amplitudes and the refractive index $n = Re(n_k)$ in the corresponding medium. Therefore, get reflectivity and transitivity

The calculation of R is on the basis of medium thickness d_m and refractive index n_k. In our circumstance, the thickness and refractive index of each layer are the experimental samples data (Fig 4.10). The constants of samples are one layer graphene placed on SiO_2/Si substrate, when the light incident on the sample from the air at room temperature (22℃), forming a 5-layer system. The refractive indexes (RI) and thickness are $n_0 = n_4 = 1$, $n_1 = n_g, d_1 = d_g$ (graphene), $n_2 = 1.41, d_2 = 300nm$ (SiO_2), and $n_3 = 3.46, d_3 = 525\mu m$ (Si), and the range of n_g extracted from Table 4-2.

The purpose of the experiments measures the reflectance of graphene multilayer structures and then combined the transfer matrix with the theorem of the relation between *k* and *n (k&n)* to derive the refractive index of graphene. The following section is the theorem method of the relation *k&n*, which is based on the universal absorption ($\alpha \approx 2.3\%$) and derived a value range of *k* depended on *n*.

1 Using fixed n_g' to calculate k_g

From the research of R. R. Nair [93] et al, that the universal absorption of graphene is α~2.3% per monolayer, and the optical property of graphene at infrared regime agrees with the universal absorption. Starting from the general equation of the definition of the absorption coefficient, when a beam propagates through an absorbing medium with extinction coefficient k and using the equation:

$$k = -\frac{\lambda}{4\pi nd} ln(1 - \pi\alpha) \tag{4-11}$$

Where *n* is real refractive index and d is the thickness of graphene, λ is incident wavelength.

Then obtain the optical index of graphene: $n_g = n_g' + i \cdot k_g$

Choose *n* range from 2.4 to 3 (reported in table 4.2), applying the relation between *k&n* derive *k* range.

$$\frac{4\pi k}{\lambda} = -\frac{1}{nd} ln\left[\frac{I}{I_0}\frac{1}{(1-R)}\right] \tag{1-12}$$

$$k = -\frac{\lambda}{4\pi nd} \ln\left(\frac{I}{I_0}\right) \tag{4-13}$$

Where R is the reflectivity, in our case the contrast should be $1-\frac{R_g}{R_s}$ R_g is the reflectivity of the sample, and R_s is the substrate reflectance at wavelength 1550nm. Results, choose n from 2.4 to 3.0, the most results from literature at wavelength 500nm-550nm.

The calculation results showed in Figure 4.10. We can see that when the value of real part of graphene RI (n) in the range of 2.4~3, derived the graphene RI imaginary section (k) is between -1.5 and -1.1, it is clear that the reported values basically agree with the published results (Table 4-2). Although the differences of the incidents wavelengths in each experiment and the unique of different samples lead to the differences, the theorem of $k\&n$ at visible and infrared regimes is valid to estimate the refractive index of graphene.

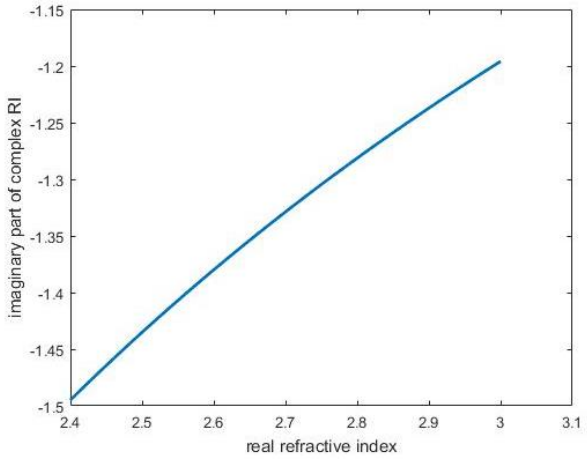

Figure 4.10 Calculation results of $k\&n$ from π-band transition and universal absorption of graphene in infrared region

4.2.3 Experimental results and discussion

The last part, we introduced the theorem of $k\&n$ as a method to estimate the range graphene refractive index. In this section, we list the optical reflectance experiments results of graphene samples to get the contrast of reflectivity ($C_R = \frac{R_g - R_0}{R_0}$). Then combined the transfer matrix of lossy medium (equation 4-5, 4-7) and $k\&n$ method to calculate the complex refractive index of graphene ($n_g = n_g' + ik_g$).

Fig 4.9 depicts the optical reflectance results of graphene samples and substrates at the same condition. The mirror reflection from 1550nm is the reference (Figure 4.11a), and different samples reflections (Figure 4.11b) shows in similar modes. Samples are monolayer graphene on top of SiO_2 thickness 300nm and Si thickness 500μm.

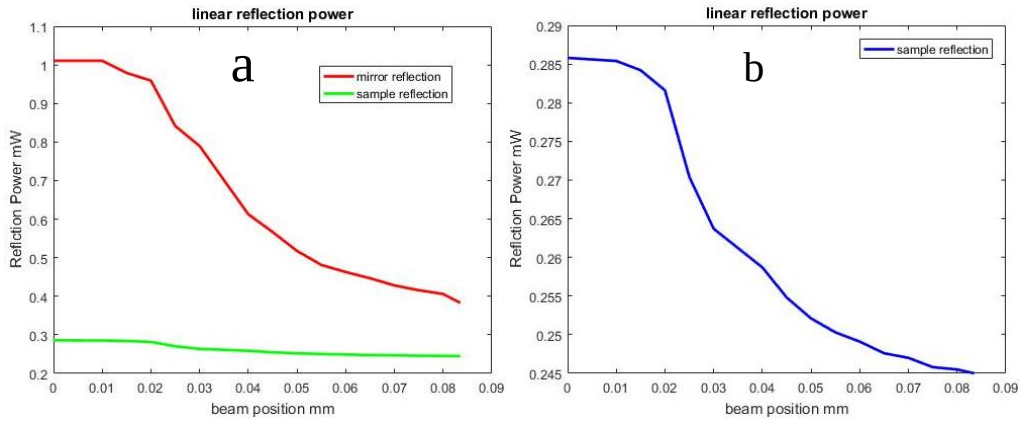

Figure 4.11 Reflection power of mirror (a) and sample1 (b) at wavelength 1550nm

In the Figure 4.11, plot (a) depicts the reflection power in Mille-Watt of both mirror and sample. Pre-set the reference reflection power at the beam waist point at 1mW, and then test the reflections at different intervals around the beam waist. Then collect the reflection data of samples at same conditions and distances. Derived the reflection power of mirrors and samples, and can see the reflections from the mirror (red line in (a)) and samples (b) behaved similarly, and both are followed the Gaussian beam power distribution.

Because of all experiments did with Gaussian beam shape, but the analysis and simulations are based on plane-wave, to derive the more precise data of refractive index of graphene especially the imaginary part, it is necessary of doing the beam construction and expansion.

From the data of mirror reflection (reference reflection) and the sample reflection (Figure 4.11), can derive the graphene/SiO_2/Si reflectivity through:

$$R_g = \frac{P_s}{P_m} \cong 0.2456 \tag{4-14}$$

And the reflection ratio of substrate is $R_0 = 0.2579$

Put both reflection coefficients of full sample and substrate, into the simulation, which used Maxwell Equation and Snell's Law mentioned in section 2.4:

$$n_g = \sqrt{\varepsilon_r} = \sqrt{1 + \frac{\sigma}{j\omega\varepsilon_0}} \tag{4-15}$$

Calculation refractive index from results

Starting from the general equation, coming from the definition of absorption coefficient, for the light through an absorbing medium with extinction coefficient κ, real refractive index n, and thickness d [97],

$$\frac{4\pi k}{\lambda} = -\frac{1}{nd} ln\left[\frac{I}{I_0}\frac{1}{(1-R)}\right] \tag{4-16}$$

Where λ is the incident wavelength, I is the transmitted light intensity, I_0 is the incident light intensity, and R is the fraction of reflected light, in our case, put experimental result ($R_s = 0.2456$) into the equation 4-16. Then, for a single graphene layer the equation can be rewritten as:

$$k = -\frac{\lambda}{4\pi nd}\ln\left(\frac{4I}{3I_0}\right) \tag{4-17}$$

From Fresnel's law, when beam paths through the interface of different material, in our case air-graphene-substrate, the definition of reflection constant (C_R) and transmission constants (C_T) are:

$$C_R = \frac{I_g - I_0}{I_0} = \frac{R_g - R_0}{R_0} \tag{4-18}$$

Where R_g, R_0 is reflectance of full sample and substrate respectively; T_g, T_0 is transmittance of entire sample and substrate respectively.

For the air-substrate effective reflection coefficient including a complex phase shift :

$$r_{02} = r_{01} + \frac{t_{01}t_{10}r_{12}e^{-i2\phi}}{1 - r_{10}r_{12}e^{-2i\phi}} \tag{4-19}$$

Where the complex phase shift through graphene of thickness ϕ is

$$\phi = 2\pi n_g \frac{d}{\lambda} \tag{4-20}$$

Where n_g is the complex refractive index of the graphene, and $\lambda = 1550nm$ is the wavelength of incident beam in our experiments. And the subscript *0* represents air, *1* represents graphene and *2* represents the substrate.

In multilayer structures, using reflection and transmission coefficient at boundaries between material a and b, express refractive indices n_a and n_b as:

$$r_{ab} = \frac{n_a - n_b}{n_a + n_b} \tag{4-21}$$

From equation (4-17) we can calculate the reflectivity of air-graphene-substrate, equation (4-21) offers the reflection of the air-substrate interface. With them, derive the reflection contrast C_R in (4-18) as a function of the real and imaginary part of the graphene refractive index, $n_g = n_g' - i\kappa_g$. The reflection ratio can be obtained from the results of the experiments, that, $R_0 = 25.97\%$; the thickness of single layer graphene using model one $d_g = 0.4nm$. And the incident wavelength is $= 1550nm$, the refractive index of substrates are $n(SiO_2) = 1.4$, thickness $d(SiO_2) = 300nm$, and $n(Si) = 3.64$, $d(Si) = 525\mu m$ Obtain the refractive index of monolayer graphene is

$$n_g = 2.78 - 1.57i \tag{4-22}$$

Compare the graphene RI value of our experiments and the reported ones (Table 4-2), we can see that the real part of the monolayer graphene is a round *2.6*, and the imaginary part is from *-1.8* to *-1.0*. And it means our result is reasonable.

Besides, according to the equations (4-5), (4-17) and (4-18), we could calculate n_g through the reflectance contrast C_R (equation (4-18)), and the transmission contrast (equation (4-24)), if we measured the optical transmission of the samples and substrates. However, because of the absorption of the substrate (SiO_2 300nm/Si 525μm) to the incident ($\lambda = 1550nm$) and the special disposed on the backside of the graphene sample, we barely detected the transmission light in our experiments. But in

the followed section, we compensate this with assumptions of absorption of the whole structure and derived another value range of graphene RI.

4.2.3.1 Using approximation of transmission to obtain n_g' and k_g

This method is deriving the monolayer graphene RI value through optical reflection and transmission ratios. According to the optical rates of lossy medium (equation 4-24), when a light propagates through a medium, the light power will split into three parts, reflection, absorption and transmission. And the transfer matrices illustrate the electric, magnetic fields changing through the reflection coefficient (equation 4-7) and transmission coefficient (equation 4-29).

$$R + A + T = 1 \tag{4-23}$$

In this method, through pre-setting the ratio of absorption (*A*) of whole graphene multilayer structures and the results in the experiment (*R*), derive the range of transmission (*T*). Then calculate the complex value of graphene RI with the reflection contrast (C_R) and the transmission contrast (C_T), with the similar process of method *1* getting the number of n_g' and k_g. Only this method does not need the relation assumption of *k&n*. With absorption range: 2%<*A*<8%, and experimental results of reflectance *Rg*=24.57%, estimate the range of transmittance *T*. then calculate complex n_g from *R* and *T*.

$$C_T = \frac{T_g - T_0}{T_0} \tag{4-24}$$

Where T_g, T_0 is transmittance of full sample and substrate respectively.

For the air-substrate effective reflection coefficient including a complex phase shift:

$$t_{20} = \frac{t_{21} t_{10} e^{-i\phi}}{1 - r_{12} r_{10} e^{-2i\phi}} \tag{4-25}$$

Where the complex phase shift through graphene thickness *d* is

$$\phi = 2\pi n_g \frac{d}{\lambda} \tag{4-26}$$

Where n_g is the complex refractive index of the graphene, and λ is the wavelength of the incident beam. And the subscript *0* represents air, *1* represents graphene and *2* represents substrate.

In multilayer structures, using reflection and transmission coefficient at boundaries between material a and b, express refractive indices n_a and n_b as:

$$r_{ab} = \frac{n_a - n_b}{n_a + n_b}, \qquad t_{ab} = \frac{2\, n_a}{n_a + n_b} \tag{4-27}$$

From equation (4-25) we can calculate the reflection of air-graphene-substrate, equation (4-29) offers the reflection of the air-substrate interface. With them, derive the reflection contrast in (4-18), as a function of the real and imaginary part of the graphene refractive index, $n_g = n_g' - ik_g$.

Full sample back side etched, therefore it is difficult to test the transmission of the sample. The absorbance assumption is from several research results [84]. Through the assumptions and calculations derived the region of graphene refractive index response to 1550nm. The Figure 4.12 shows the calculation results when assuming the sample absorptions from 2% to 8%. The assumption is from the researches of monolayer graphene absorbs around 2% of the infrared light range, and absorptions of SiO_2 varies from 1% to 6% due to different thickness and the doping levels [82]. Through the estimate region of absorption get the region of transmission and obtain the limits of the refractive index of graphene.

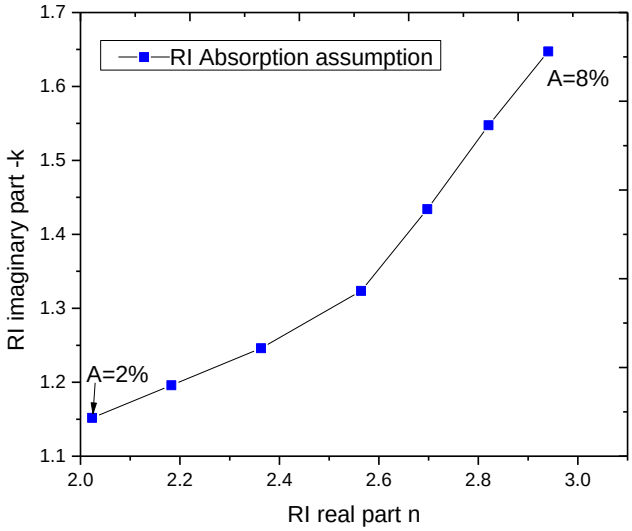

Figure 4.12 The calculation results of k and n at different absorption assumptions from 2% to 8%, through transfer matrix.

4.2.4 Discuss and Conclusion

We performed optical reflectance on CVD mono-layer graphene samples under wavelength 1550nm laser. The optical index of the few-layer graphene flakes was determined based on their contrast to the bare SiO_2/Si substrate by using Fresnel theory of reflection and transmission to the air/graphene/SiO_2/Si multilayer.

The summary of the two methods is below in Figure 4.13. From the graph, the methods of the universal absorption relation of k verses n (black square line), and the assumption of sample absorptions (green triangle line) apply the value regions of graphene refractive index. The red spot in between is the calculation result of the refractive index of graphene derived from reflection spectroscopy of graphene/SiO_2/Si sample under incident 1550nm, obtained the RI value is $n_g = 2.75 - 1.56i$. The spectral results are between the two assumptions regions, which means the reflection results are reasonable. The reflection and transmission calculation based on the assumption of absorption of the medium, for specific graphene samples, the values of refractive index are not entirely precise. But still, the curve gives an acceptable RI range of single-layer graphene. The method of k&n derived from the universal absorption of monolayer graphene, which provides a simple way to describe the optical behavior of graphene (equation 4-14).

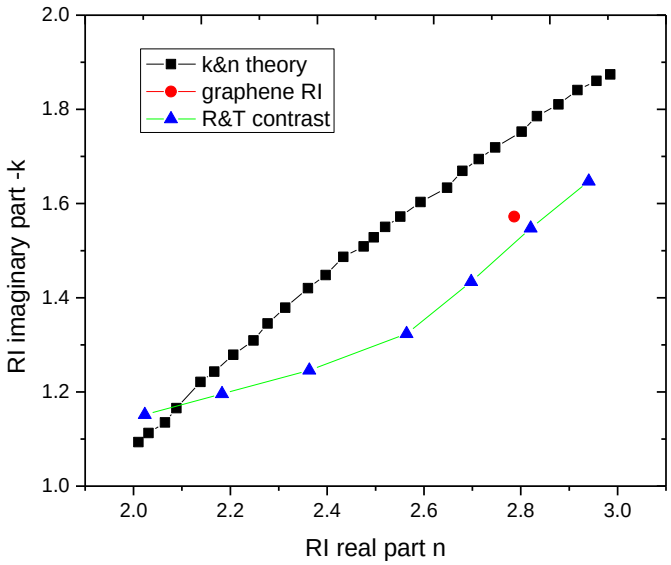

Figure 4.13 The region of complex refractive index of graphene and the calculation results matching. The red spot in the 2nd method is the experimental results from graphene sample reflection spectra without external electric field.

Table 4-3 illustrates the comparison between the calculation results and a theoretical research by L. Yang *et al* [87]. The article presented optical response on bi-layer graphene, and they calculated the conductance of bi-layer graphene with Green's function theory. We can see from the Figure 4.14, when $n \leq 2.8$, bi-layer graphene imaginary part is larger mono-layer graphene. Yang *et al*' s research was working on pure bi-layer graphene, there are inevitable differences between experiments and theory (shown in Figure 4.11).

Table 4-3 Theory compares in refractive index range of graphene

reference	Method	Material	wavelength	Figure 4.14
Current work	Reflection with k&n	1L graphene SiO_2 300nm Si 525μm	1550nm	Black
	Reflection and transmission	1L graphene SiO_2 300nm Si 525μm	1550nm	Red
Yang *et al* [87]	Full band theory	2L graphene	550nm	Blue

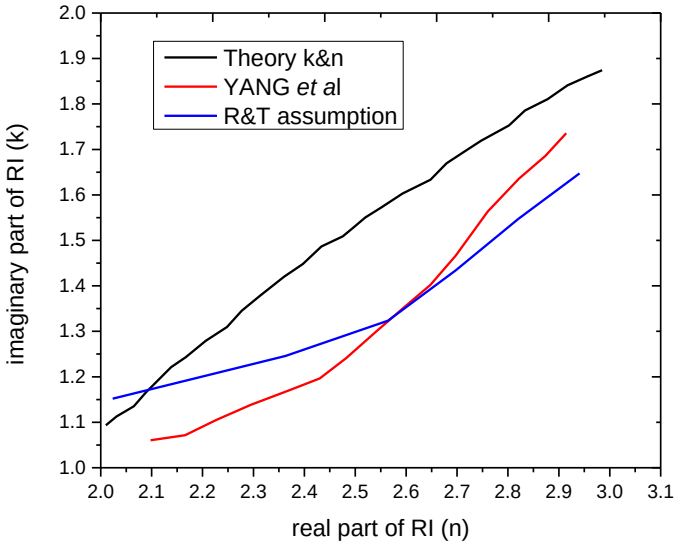

Figure 4.14 Graphene RI calculation methods in our work compared with a reported one (Yang *et al)* [87].

We present a further comparison (Figure 4.15) of our experimental results and various of optical constants for graphene and graphite in the literature. All optical constants are compared here in the form of optical refractive index per graphene layer. The experimentally constrained RI of graphene in literature was found numerically calculating via Fresnel theory with the optical reflection contrast measured at visible range. Wherever, there is a lack of similar measurement in the infrared range, and our experiments fill the gap of graphene optical reflection and transmission.

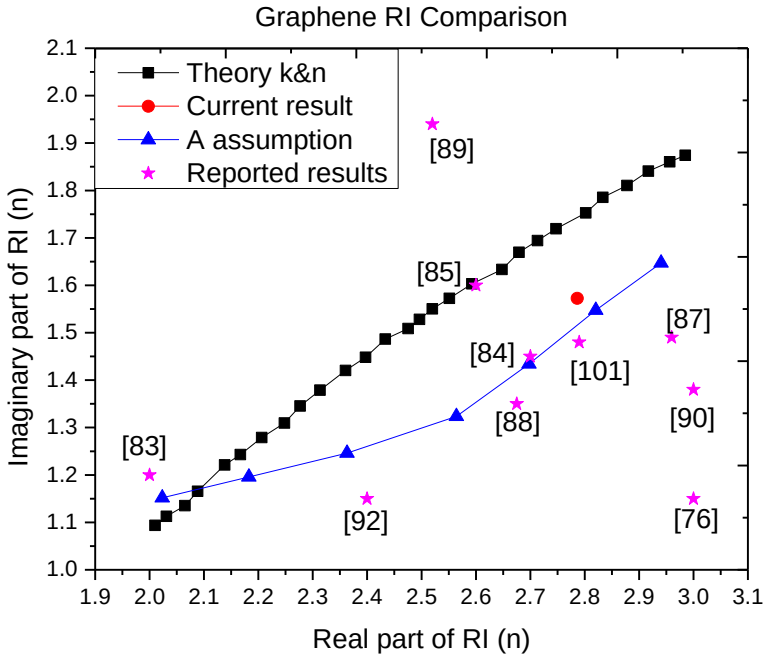

Figure 4.15 Comparison of various optical values for graphene with a different method at the divers laser wavelength. Star symbols values obtained from literatures.

We see in Figure 4.15, in the comparison of our experimental refractive index and reported values of optical constants. The full band calculations of Ahuja *et al* [90] and Klitenberg *et al* [100] overestimate the real part of RI. Similarly, the experimentally reported value or RI for graphite by Jellison *et al* [89] predicts a larger substantially imaginary region, which means more optical absorption per graphene layer than the universal absorption results [91]. Besides, the difference between reflection results can be influenced by the material and thickness of the substrates, and again lead to the various of graphene RI. With a potential application of graphene being highly transparent and highly conductive electrodes, the optical reflection and transmission properties of graphene merit detailed attention. The relative insensitivity of optical reflection and transmission to the imaginary optical constants in thin graphene film is an advantage for both modeling and optical application.

4.3 Gated graphene refractive index tunability

4.3.1 Introduction

High conductivity [93] and low optical absorption [80-82] make graphene an attractive material for use as a flexible transparent conductive electrode. This atomically carbon layer thickness provides the significant sensitivity of material conductance that its work function can be adjusted by the electric field effect (EFE). Since their respective work functions determine the band alignment of two different materials, control over the graphene work function is the key to reducing the contact barriers of graphene top electrode devices [105]. Previous scanning probe based studies [96] reveal that the work function of graphene is in a similar range to that of graphite, ~4.6 eV [97], and depends sensitively on the number of layers [98]. However, the active controlling of the graphene work function has yet to be demonstrated.

In the former section, we .measured optical refractive index of monolayer graphene on SiO_2/Si. As a semi-conductive material [102], the changes of the electrical property has effects on optical properties (shown in equations (4-9), (4-10)). Owing to the low density of states, the chemical potential in graphene can be modulated by external gate voltage to populate electrons to the conduction band or remove electrons from valence band. Therefore, the tunability of chemical potential determines the electrically operating optical transition on graphene-based devices. This unique property enables graphene applied in high-frequency field effect transistors (FETs) [108]. The optical application of graphene is also excellent, such as gas sensors [104], optical resonators [105] and modulators [106].

In this section, we test the reflection contrast response to the external gated voltage changing to evaluate the relationship between graphene refractive index and chemical potential.

4.3.2 Electronic model of graphene

In graphene, the energy-momentum relationship is linear at the Dirac points (see Figure 2.3) over a wide range of energies. Thus electrons in graphene behave like massless relativistic particles with an independent energy velocity. The two cone band structure of graphene together with the extreme thinness leads to a variety of material's carrier concentration with static electric gating [109]. This effect enables to develop ultrathin carbon nanoelectronic devices. Furthermore, it has been shown that conductance of graphene has a minimum, non-zero value associated with the conductance quantum, even when charge carrier concentrations vanish [110].

Monolayer graphene for the optical experiment can modele as a conductivity sheet (shown in Figure 4.17) (0.4nm-2nm), when a beam with frequency ω_p incident on it, will generate a surface current J_k which will be the electric field source, given:

$$J_k = \bar{\bar{\sigma}}^{(1)}_{intra}(k, \omega_p) \cdot E \tag{4-28}$$

Where $\bar{\bar{\sigma}}^{(1)}_{intra}(k, \omega_p)$ is the intraband conductivity in k-space; k is the wave number of the incident electric field; E is the incident electric field $\mathrm{E} = \tilde{E}_p \exp(i\omega_p t)$.

Derive the intraband conductivity in linear part from Kubo formula [109]:

$$\sigma_{intra}(\omega_p) = \frac{e^2}{\hbar}\frac{g_s g_v}{4\pi}\frac{k_B T}{\hbar(i\omega_p+\Gamma)} \times \left[\frac{\mu_c}{k_B T} + 2ln\left(1 + e^{-\mu_c/k_B T}\right)\right] \tag{4-29}$$

is the master equation of the optical response of single-layer graphene. In equation (4-29), g_s, g_v are spin and valley degeneracy factors respectively, here the values are $g_s\ g_v = 4$; e is the electron elementary charge, k_B is the Boltzmann Constant, T is Kelvin temperature, Γ is Landau level index dependent scattering rate [109], which is a constant here, $\hbar\Gamma = 0.1\mathrm{eV}$; $\hbar = \frac{h}{2\pi}$ is Plank Constant; μ_c is the chemical potential of graphene. Then simplify the intraband conductivity to be:

$$\sigma_{intra}(\omega_p) = \frac{e^2 k_B T}{\pi\hbar^2(i\omega_p+\Gamma)}\left(\frac{\mu_c}{k_B T} + 2ln\left(e^{-\frac{\mu_c}{k_B T}} + 1\right)\right) \tag{4-30}$$

From the linear process of single photon active [112]. The first order of the equation can be derived from K-space to ω-space.

$$\overline{\overline{\sigma_{inter}}}(k, \omega_p) = \frac{e^2}{\hbar}\frac{v_F}{\sqrt{k^2+(\delta k)^2}}\frac{(\gamma_2+i\omega_p)w_k^{eq}}{\omega_p^2-2i\gamma_2\omega_p-\Omega_k^2}[f(\varepsilon) - f(-\varepsilon)] \tag{4-31}$$

Where k is the incident wave number, v_F is the Fermi velocity, γ_2 represents the frequency dependent impurity scattering rate [109], where its value is $\hbar\gamma_2 \cong 0.01eV \sim 0.1eV$, $f(\varepsilon)$ is the Fermi level of the graphene band structure. Assume the energy of incoming photons is normalized to the Fermi energy.

The simulation results of the linear conductance are shown in Figure 4.17. It is

observed that the optical absorption of monolayer graphene is universal and independent to the incident frequency when the photon energy $\hbar\omega_p > 2E_f$.

When a plane wave is an incident on a monolayer graphene, the graphene behaves like a sheet of metal.

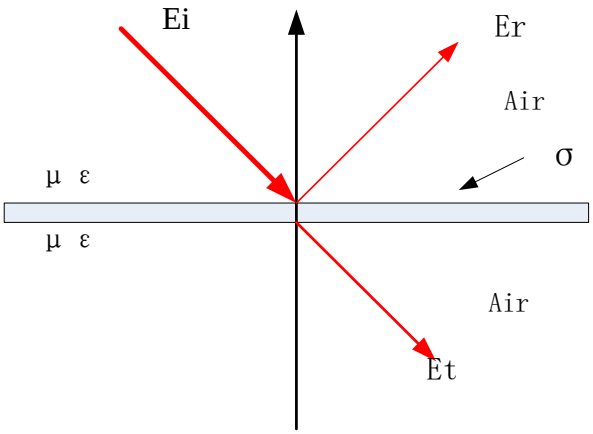

Figure 4.16 Graphene characterized by conductance σ at the interface in the air.

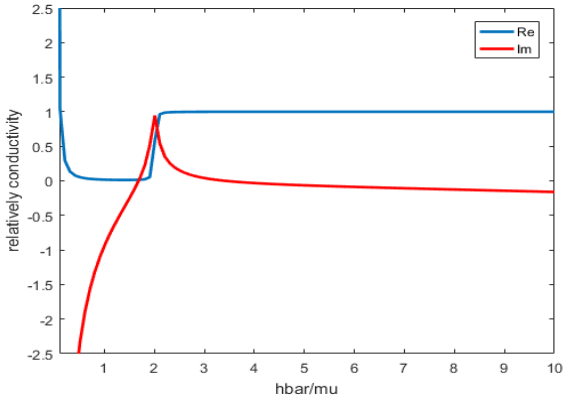

Figure 4.17 Linear optical conductivity of graphene for a normally incident plane wave. The parameter $\sigma_0 = e^2/(4\hbar)$ is the universal optical conductivity. $\hbar\omega_p/E_f$

The theoretical model of graphene is an infinitesimally-thin due to its atomic thickness, local two-sided surface characterized by a surface conductivity σ, and the complex conductivity can be expressed from Kubo formula [112],

$$\sigma(\omega,\mu_c,\Gamma,T) = \frac{je^2(\omega-j2\Gamma)}{\pi\hbar^2}\left[\frac{1}{(\omega-j2\Gamma)^2}\int_0^\infty \varepsilon\left(\frac{\partial f_d(\varepsilon)}{\partial\varepsilon}-\frac{\partial f_d(-\varepsilon)}{\partial\varepsilon}\right)d\varepsilon - \int_0^\infty \frac{f_d(-\varepsilon)-f_d(\varepsilon)}{(\omega-j2\Gamma)^2-4(\varepsilon/\hbar)^2}d\varepsilon\right] \quad (4\text{-}32)$$

Where ω is radian frequency, μ_c is chemical potential determined by charge accumulation on graphene, Γ is a phenomenological scattering ratio that is $\hbar\Gamma = 5mV$ independent of energy ε [106], and T is temperature; e is the electron charge, $\hbar$ is the reduced Plank's constant, $f_d(\varepsilon) = \left(e^{(\varepsilon-\mu_c)/k_BT}+1\right)^{-1}$ is the Fermi-Dirac

distribution. k_B is the Boltzmann's constant. The first term in equation (4-32) represents intraband contribution, and the second term is due to interband contribution.

For an isolated single-layer graphene sheet, the electrical chemical potential μ_c is determined by carrier density n_s [107]:

$$n_s = \frac{2}{\pi\hbar^2 v_F^2}\int_0^\infty \varepsilon\big(f_d(\varepsilon) - f_d(\varepsilon + 2\mu_c)\big)d\varepsilon \tag{4-33}$$

Where v_F is the Fermi velocity. The carrier density can be controlled by the applied gate voltage and/or chemical doping. In our experiments, we applying a voltage V to the graphene layer and the sheet carrier density n_s is approximated as an ideal parallel-plate capacitor:

$$n_s = \frac{C_{SiO_2}|V_G - V_D|}{e} \tag{4-34}$$

Where C_{SiO_2} is the gate capacitance per unit area of the gated graphene sample, and V_D is the threshold voltage, which is Dirac voltage in our experiments. Therefore, the chemical potential μ_c can be written as [108]:

$$\mu_c = \hbar v_F\sqrt{\pi(n_s)} = \hbar v_F\sqrt{\pi\left(\frac{C_{SiO_2}|V_G - V_D|}{e}\right)} \tag{4-35}$$

The value of chemical potential μ_c can be varied by an applied external gate voltage V_G through the silicon dioxide capacitance between the graphene and silicon substrate:

$$\mu_c = \hbar v_F\sqrt{\frac{\pi\varepsilon_{ox}}{ed_{ox}}(V - V_D)} \tag{4-36}$$

Where ε_{ox} and d_{ox} are the dielectric constant and the thickness of SiO_2 layer respectively, V_D is the Dirac Voltage determined by the unintentional doping of graphene from the substrate and surrounding environment. $v_F \approx 0.8 \times 10^6 m/s$ is the Fermi velocity (see section 2.2), which is dependent to the substrate.

4.3.3 Experiment and results discussions

4.3.3.1 Experiments and Results

The experiment did at room temperature. Figure 4.18 shows the sketch of setup. A femtosecond pulse laser at 1064nm wavelength was used in the experiment with spectral linewidth of approximately 40MHz. The laser output was collimated into the system and focused on the sample through the self-designed focal system (see section 4.1.1), and the focused spot diameter on the sample was around $5\,\mu m$. The reflected beam passing through beam a splitter and detected by a photodetector. A microscope was inserted to observe the position of the beam spot on graphene sample. A lock-in amplifier was used to improve the signal-to-noise ratio. Optical signal modulation for synchronizing the lock-in amplifier could be applied either through a mechanical chopper or a modulation on the gate voltage of the sample. A computer was used to control the motion of translation stage, to adjust gate voltage and to acquire data from power-meter and a lock-in amplifier, Figure 4.19 depicts the real setup.

.

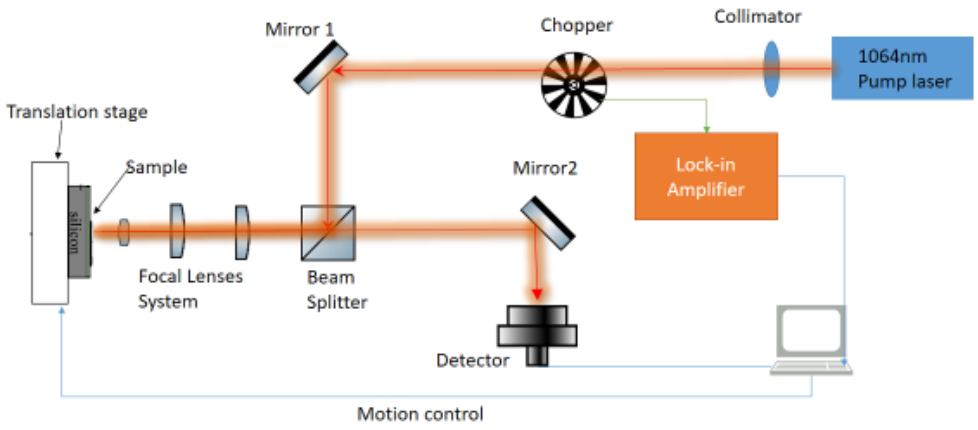

Figure 4.18 Sketch of gated graphene reflection spectroscopy

We measured the optical power reflectance R varies with the linear changed external gate voltage on graphene sample, the position of the laser beam fixed on the same spot on graphene sample. As this variation was expected to be less than 1%, the system had to be stable enough, and the impact from laser power variation and interference caused by reflections from various optical components in the system had to minimize. Thus, in this measurement, the frequency mechanical chopper controlled by the amplifier to synchronize the lock-in amplifier. An adjustable DC gate voltage was added to the small-signal modulating waveform through a bias-tee as illustrated in Figure 4.22. This is equivalent to a small-signal modulation on chemical potential of the graphene, and therefore the lock-in amplifier actually measures the differential reflectivity $\delta R(V)/\delta V$.

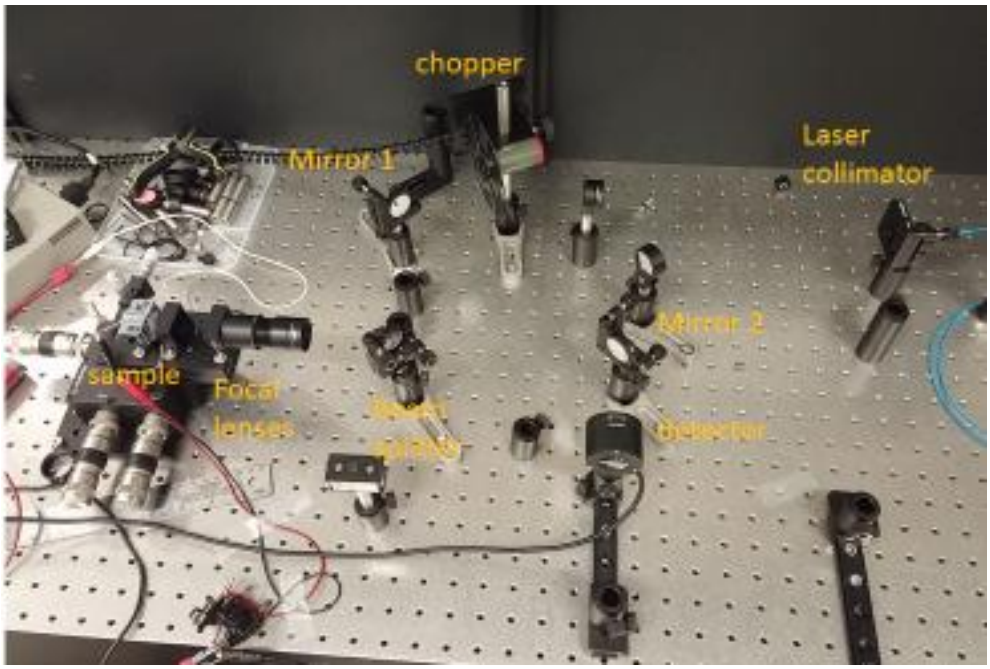

Figure 4.19 Tunability of gated graphene refractive index setup

Figure 4.20 shows the differential reflectivity measured on the graphene when the DC bias voltage was linearly ramped up and down between -27V and 23V, and the rate of this voltage scan was approximately 1V/s. We observed the reflection varies dependent on gate voltage changing was not directly perceived. The tunability of graphene complex reflectivity is not a linear function of the applied gate voltage. The experimental results also dependents on the optical interference of the multi-layered structure of SiO_2/Si and the thickness of each layer.

The light path of the tunability test is similar to the reflection one, the only two differences are:

i. Adding a mechanical chopper to provide a incident frequency reference to in-lock amplifier;

ii. No beam profiler;

The small bias voltage between source and drain terminals is 0.2V, provide by in-lock amplifier;

The gate voltage comes from a DC supply.

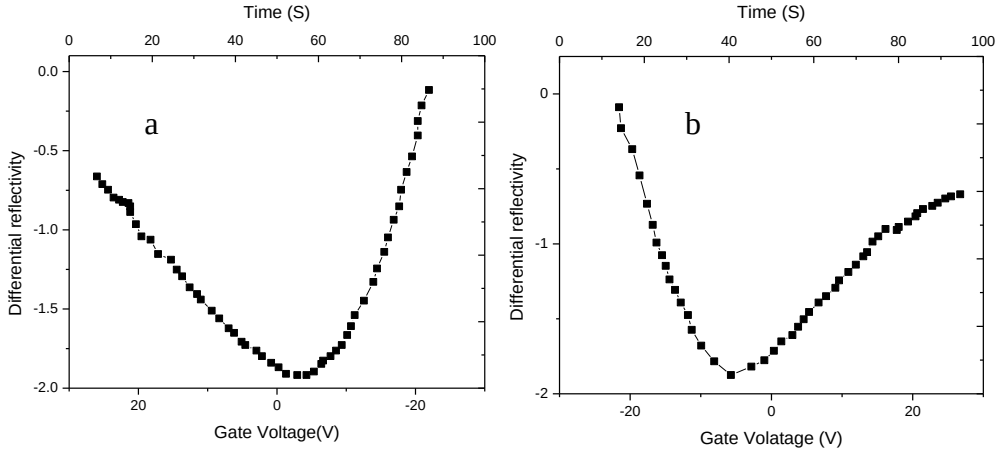

Figure 4.20 Differential reflectivity change with continues decreasing (a) and increasing (b) gate voltage on top-gated graphene/SiO_2/Si

4.3.3.2 Discussions

Another observation of Figure 4.21 is that $\delta R(V)/\delta V$ depends on the direction of voltage scan, and this hysteresis is attributed to the charge trapping and storage in graphene. The gate dependence of these optical transitions provides an extra dimension of information. For a given photon energy, the absolute value of gate voltage $\delta R(V)/\delta V$ has a maximum at a particular gate voltage, as can be seen from a vertical cut of the plot.

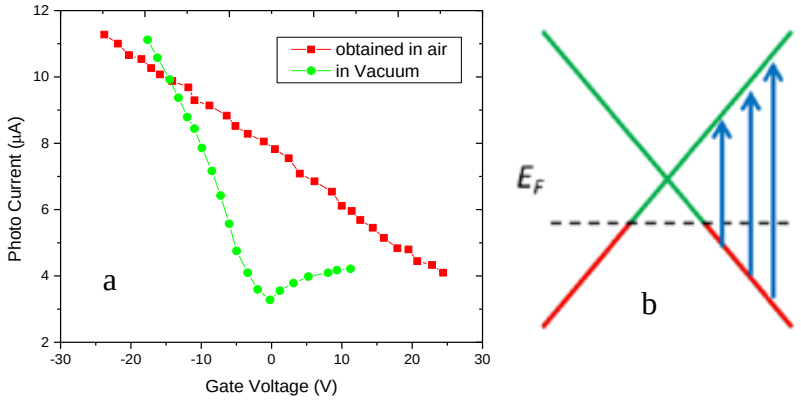

Figure 4.21 a. Source-Drain current varies with gate voltage change curves taken on a typical graphene structure in the air (red line) and in the vacuum (green line). b. Interband transition in monolayer graphene. E_F shifts upon gating.

We observed that when graphene sample was exposed to the open air, V_D might increase dramatically [113, 114]. Figure 4.21 shows characteristic curves of source-drain current, I_{SD}, as the function of the gate voltage measured in a FET device made of the same batch of graphene on the SiO_2(300 nm)/Si wafer. Although the V_D value corresponding to the minimum of I_{SD} was approximately zero when the sample placed in the vacuum [114], V_D moved beyond the measurable voltage window after the sample was exposed to the air. The maximum applicable gate voltage was primarily limited by the effective dielectric strength of silicon oxide of -0.5V/nm [115], corresponding to about $\pm 40V$ in this case. A consistent result obtained on more than ten similar FETs. Because our optical characterization performed in the open air under ambient conditions, the Dirac point was expected to be in exceeding 45V [120].

The spectra of graphene monolayers allow us to determine the electronic band dispersion. We consider the interband transitions illustrated in the Figure 4.22 b. The applied gate voltage changes the charge-carrier density in graphene, $N = \delta \cdot V$, and accordingly shifts E_F, where $E_F = sgn(N)\hbar v_F \sqrt{\pi |N|}$. Here, positive or negative N represents electron or hole respectively. v_F is the Fermi velocity, $\delta \approx 7 \times 10^{10} cm^{-2} V^{-1}$ (estimated from a simple capacitor model [116]). The shift E_F affects IR spectrum through the Drude response of the altered electron density and through the change of band filling (such as a downshift of E_F eliminates transitions originating from initially occupied states right above the downshifted E_F).

The band-filling effect dominates at photon energy corresponding to transitions that originate from states near the Fermi surface, that is $2|E_F| = \hbar\omega$. Based on the discussion presented by F. Wang *et al* [115]. The maximum reflectivity tendency ∂(dR/R)/∂V signal is defined by $\hbar\omega = 2\hbar v_F \sqrt{\delta\pi |V|}$, and the slope of $(\hbar\omega)^2$ versus V yields directly the dispersion velocity of the Dirac band, $v_F \approx 0.8 \times 10^6 m/s$ (Figure 2.3). Our value is comparable to that obtained by transport [99] and by photoemission [117-119], and the small difference could be due to the uncertainty in our determination of gate-coupling efficiency. To describe the gate-dependent spectra quantitatively,

calculating the complex linear conductivity and optical transition from Kubo theorem with graphene band structure tight-binding model [104, 105] at different Fermi levels (E_F). In this model, the velocity of Dirac band v_F is the only parameter needed to describe the band structure and optical transfer matrix elements, and V determines the Fermi energy level.

To probe optical transitions of graphene monolayers, we measured the normalized change of IR reflectivity $\delta R/R$ from the sample concerning the bare substrate, achieved by scanning the reflection ratio changings between the full sample structure and the bare substrate film. Note that the $\delta R/R$ is related to the complex optical conductivity $\sigma(\omega)$ of graphene through the relation:

$$-\frac{\delta R}{R} = \frac{1}{c} Re[\eta \cdot \sigma] \tag{4-37}$$

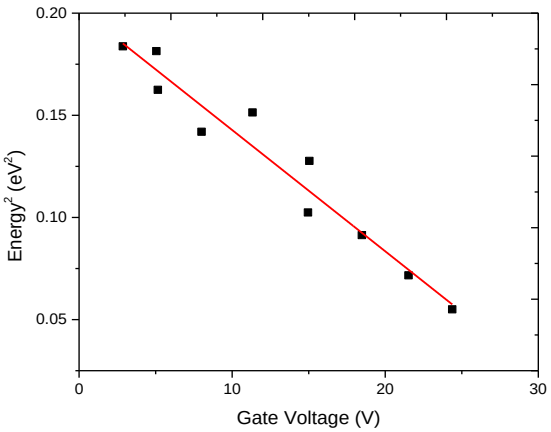

Figure 4.22 The trace of maximum modulation plotted as squared photon energy versus gated voltage. The function shows linearly with gate voltage, the phenomenon represents the Fermi velocity v_F is a constant.

From former section, the relationship between refractive index and conductivity (see formula $n_g = \sqrt{\varepsilon_r} = \sqrt{1 + \frac{\sigma}{j\omega\varepsilon_0}}$) also works in the gate-dependent conditions. The normalized change of the power reflectivity on the sample surface without and with the graphene can be calculated based on the multilayer interference theory as [120]:

$$\frac{\Delta R}{R_0} = \pi d_g \cdot Re\{(1 - n_g^2)(1 + r_0)^2/(r_0\lambda)\} \tag{4-38}$$

Where R_0 is the optical reflectivity of the substrate without graphene, d_g is the thickness of graphene, n_g is the refractive index of graphene, λ is the incident wavelength. For the sample we used in the experiment, the substrate SiO_2/Si:

$$r_0 = \left(r_{01} e^{j\beta_{ox} d_{ox}} + r_{12} e^{-j\beta_{ox} d_{ox}}\right) \Big/ \left(e^{j\beta_1 d_1} + r_{01} r_{12} e^{-j\beta_{ox} d_{ox}}\right) \tag{4-39}$$

$$R_0 = |r_0|^2 \tag{4-40}$$

Where, $\beta_{ox} = 2\pi n_{ox}/\gamma$ is the propagation constant of the SiO_2 layer; $r_{01} =$

$(n_{ox}-1)/(n_{ox}+1)$ and $r_{12}=(n_s-n_{ox})/(n_s+n_{ox})$ are Fresnel reflectivities at air/SiO_2 and SiO_2/Si interfaces respectively, with n_{ox}=1.4 and $n_s=3.46$ refractive indices of SiO_2 and Si.

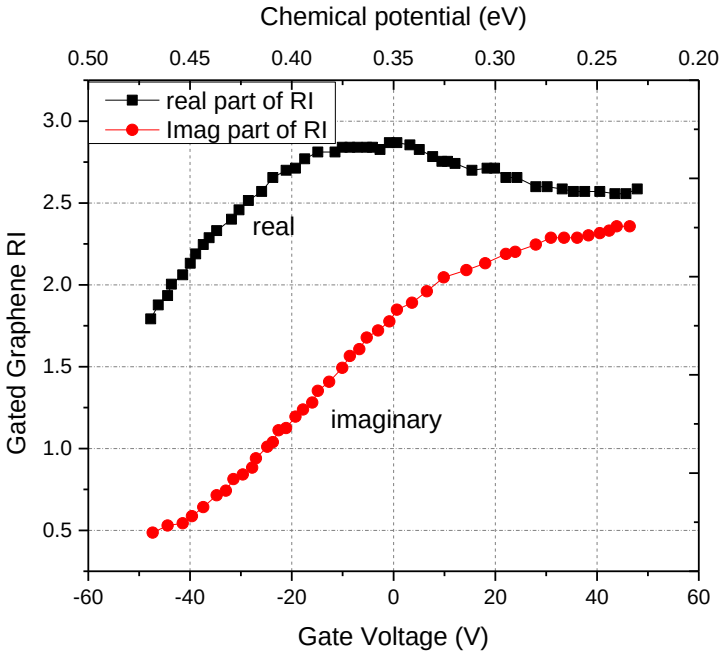

Figure 4.23 Complex refractive index change with different gate voltage according to experimental results. Top-gated graphene sample monolayer graphene on SiO_2/Si substrate under 1064nm laser beam

Figure 4.23 illustrates the real and imaginary part of the graphene refractive index as the function of chemical potential from equation (4-35) the bottom horizontal axis is gate voltage, which is related to the chemical potential from equation (4-36). We used V_D=65V and d_{ox}=300nm to obtain the best fitting for the measured result. Besides, from the plot, when the gate voltage equals zero, means no external voltage applied to the sample, the values of real and imaginary parts are n_g'=2.81 and k_g=1.78 respectively. This value is similar to the former reflection experimental results n_g'=2.75 and k_g=1.57, which performed under 1550nm laser (showed in Figure 4.13). The optical index value of graphene at zero voltage points founds that different incidents can determine refractive index monolayer graphene, the amount grows with longer incident wavelength. Further, the various gates and SiO_2/Si substrate thickness also have influences on the graphene RI value. The difference between the two results isvarious mainly from the different incident wavelengths.

F. Xu *et al* [120] reported a similar work that measuring the reflectivity change on graphene when applied constant increasing gate voltage. The substrate of their sample is SiO_2 (90nm) and Si as the back gate, the incident is from 1550nm continuous laser. And the complex refractive index results is larger than ours (shown in Figure 4.24). From the Figure 4.24, we can see that the real part of the RI has about 0.4 difference between the two experiments but the imaginary parts are almost same for two tests.

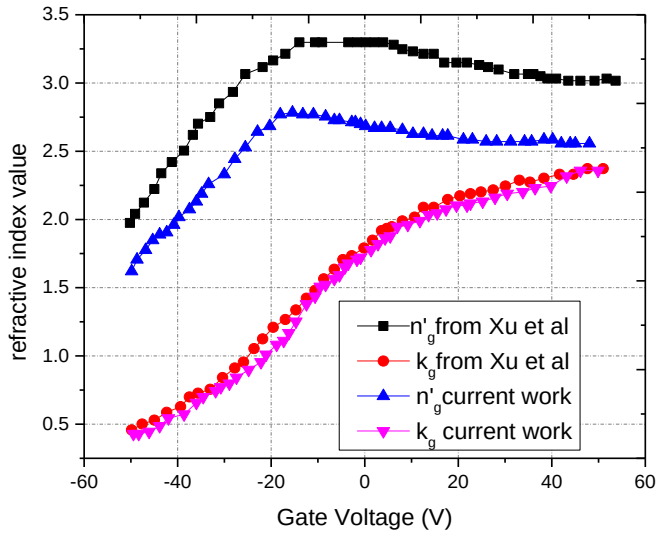

Figure 4.24 Refractive index values compare between F. Xu [120] group work (λ=1550nm) and current experiments (λ=1064nm).

4.3.4 Conclusion

In summary, the reflectivity variation across the edge of CVD graphene on a SiO_2 (300 nm)/Si substrate measured at 1064 nm optical communications wavelength. The measured change of reflection as the function of applied gate voltage agrees reasonably well with the theoretical prediction based on modeling using the Kubo formula. We verified the tunability of complex refractive index of graphene, which is the most important parameter for the design of graphene-based photonic devices for optical communications.

5 Conclusions

Graphene is found to be an excellent material for the optoelectronic applications, due to its unique optical, electrical, and mechanical properties. The optical properties have been studied intensely due to their extraordinary transmission response to different optical regions (from Terahertz to infrared). This thesis has obtained the complex refractive index of monolayer graphene through optical reflection measurements.

The optical absorption of graphene varies in response to different substrates and doping conditions. Therefore, we started with the graphene sample syntheses in our experiments, which described in chapter 3. Monolayer graphene was fabricated with chemical vapor deposition (CVD) methodology, grown on commercial copper and then transferred onto a SiO_2/Si wafer. Top gate samples implemented with atomic layer deposition on graphene samples.

The optical reflection experiments described in chapter 4, included (i) the setup design, (ii) reflection tests on graphene/SiO_2 (300nm)/Si (525μm) samples under the 1550nm laser, and (iii) gated graphene reflection tunability under a 1064nm laser.

The optical refractive index of graphene was derived from the reflection test results on graphene samples through transfer matrices method, and obtained the real part n_g' range from *2.4* to *3.0*, and imaginary part k_g is between *-1.5* and *-1*, respectively. We compared this value range with several reported results proved the range can describe the optical property well. We also introduced a theoretical method "*k&n*" to estimate the complex value of graphene RI. This method is based on the proved universal optical absorption of single-layer graphene. Combining the above methods, we obtained the complex monolayer graphene RI $n_g = 2.75 - 1.56i$, at 1550nm.

Graphene is a semi-metal due to its zero-gap band structure, which is sensitive to variations of the energy potential change. The sensitivity of graphene's conductivity to an applied gate voltage influences its refractive index of optical frequencices. Therefore, our reflection tunability experiments tested the top-gated graphene optical response to the electrical field changes. We checked the photocurrent change with continuous increasing gate voltage as the characterization of the gating, then compared this change with results under the vacuum condition. The photocurrent descended linearly with increases gate voltage, which was slower than one at vacuum condition. Then we presented the Fermi energy level change to increasing gate voltage, which satisfied with the energy level of field-effect transistors (FET). The change of the gate voltage enables the top-gated graphene sample as a GFET.

How graphene RI changes with increasing gate voltage was calculated through the graphene band structure model and derived that when the gate voltage was continuously growing from -50V to 50V. The real part rises before 0V and descends slowly after, and reached the peak at n_g'=2.81. But the imaginary part rises continuously, and when the gate voltage is 0V, the value is k_g=1.78, which is near to the former results. The small difference arises from the different incident wavelength. We also compared our results with a reported one [120]. Graphene RI's tendency to change in both studies is similar

(Figure 4.24), differences between values are mainly due to the different samples and incident wavelengths. We can see that the imaginary parts in the two are similar, which illustrates that the optical absorption of graphene is stable.

The work has been focused on graphene's linear refractive index measurement through reflectometry setup. The next step would be to generalize the characterization to both reflection and transmission measurements to obtain more accurate values of graphene RI. Then this configuration can also be used to characterize the nonlinear refractive index of graphene, namely the Kerr effect.

References

[1]. Y. M. Lin, C. Dimitrakopoulos, K. A. Jenkins, D. B. Farmer, H. Y. Chiu, A. Grill, and Ph. Avouris. "100-GHz transistors from water-scale epitaxial graphene". Science 327:662. (2010).

[2]. K. S. Kim, Y. Zhao, H. Jang, S. Y. Lee, J. M. Kim, J. H. Ahn, P. Kim, J. Y. Choi, and B. H. Hong. "Large scale pattern growth of graphene films for stretchable transparent electrodes". Nature 457: 706-710. (2009).

[3]. L. G. de Arco, Y. Zhang, C. W. Schlenker, K. Ryu, M. E. Thompston, and C. Zhou. "Continuous, highly flexible and transparent graphene films by chemical vapor deposition for organic photovoltics". ACS Nano 4: 2865. (2010).

[4]. N. Yang, J. Zhai, D. Wang, Y. Chen, and L. Jiang. "two dimensional graphene bridges enhanced photo-induced charge transport in dye-sensitized solar cells". ACS Nano 4: 887. (2010).

[5]. C. S. Shan, H. F. Yang, D. X. Han, Q. X. Zhang, A. Ivaska, and L. Liu. "Graphene/AuNPs/chitosan nanocomposites film for glucose biosensing". Bioelectron. 25, 1070. (2009).

[6]. I. Lahiri, R. Seelaboyina, Y. G. Hwang, R. Banerjee, and W. Choi. "Enhanced field emission from multi-walled carbon nanotubes grown on pure copper substrate". Carbon 48: 1531-1538. (2010).

[7]. S. Ghosh, D. L. Nika, E. P. Pekatilov, anf A. A. Balandin. "Heat conduction in graphene: Experimental study and theoretical interpretation". New Journal of Physics 11:095012. (2009).

[8]. K. S. Novoslov, A. K. Geim, S. V. Moro Zov, D. Jiang, Y. Zhang, S. V. Dubonos, I. V. Grigorieva, and A. A. Firsov. "Electric effect in atomically thin carbon films". Science 306 (5696):666-669 (2004).

[9]. J. Wu, H. A. Becerril, Z. Bao, Z. Liu, Y. Chen, and P. Peumans. "Organic solar cells with solution-processed graphene transparent electrodes". Applied physics Letters 92(26):263302-3 (2008).

[10]. A. K. Geim and K. S. Novoselov. The rise of graphene, Nature Materials, vol 6 (3), 183-191 (2007).

[11]. A. H. Castro Neto, F. Guinea, N. M. R. Peres, K. S. Novoselov, and A. K. Geim. The electronic properties of graphene. Rev. Mod. Phys., 81:109–162, Jan （2009）.

[12]. P. R. Wallace. " The band theory of graphene". Physical Review 71: 662. (1947).

[13]. Y. B. Zhang, Y. W. Tan, H. L. Stormer, P. Kim, Experimental Observation of the Quantum Hall Effect and Berry's Phase in Graphene. Nature, 438, 201–204 (2005).

[14]. J. C.Meyer, A. K. Geim, M. I.Katsnelson, K. S.Novoselov, T. J.Booth, S.Roth, The Structure of Suspended Graphene Sheets. Nature, 446, 60–63(2007).

[15]. Han, M. Y.;O ¨ zyilmaz, B.; Zhang, Y.; Kim, P. Energy Band-Gap Engineering of Graphene Nanoribbons. Phys. Rev. Lett., 98, 206805(2007).

[16]. Adam Rycerz, Random matrices and quantum chaos in weakly disordered graphene nanoflakes Phys. Rev. B 85, 245424 (2012).

[17]. E.G.Sauter *Nonlinear Optics,* A WILEY-INTERSCIENCE PUBLICATION, 1996.

[18]. Giampiero Contestabile, Akihiro Maruta and Ken-Ichi Kitayama, Four wave mixing in quantum dot semiconductor optical amplifier, IEEE JOURNAL OF QUANTUM ELECTRONICS, VOL. 50, NO. 5, MAY 2014.
[19]. H. Zhou, T.Y.Gu, J. F. McMillan, N. Petrone, A.V.F.Zande, J. C. Hone, M.B.Yu, etc. Enhanced four wave mixing in graphene-silicon slow light photonic crystal waveguides, APPLIED PHYSICS LETTERS 105, 091111, 2014.
[20]. K. Hazu, S. F. Chichibu, S. Adachi and T. Sota, *valence-band-ordering of a strain-free bulk single ZeO crystal identified by four wave mixing spectrapy technique.* JOURNAL OF APPLIED PHYSICS 111, 093522 (2012).
[21]. [Land, T.A., Michely, T., Behm, R.J., Hemminger, J.C., Comsa, G. STM investigation of single layer graphite structures produced on Pt(111) by hydrocarbon decomposition. *Sur. Sci.* **264**, 261-270 (1992).
[22]. Novoselov, K. S., Geim A. K., Morzov S. V., Jiang D., Zhang Y., Katsnelson M. I., Grigorieva I. V., Dubonos S. V., and Firsov A. A. two-dimentinal gas of massless Dirac fermions in graphene. Nature 438:197-200. (2005).
[23]. Ohta T., Bostwick A., Seyller T., Horn K., and Rotenberg E. Controlling the electronic structure of bilayer graphen. Science 313:951. (2006).
[24]. Feldman B. E., Martin J., and Yacoby A. Broken –sysmmetry states and divergent resistance in suspended bilayer graphene. Nature Physics 5: 889-983. (2009).
[25]. Gozalez J. W., Santos H., Pacheco M., Chico L., and Brey L. Electronic transport through bilayer graphene. Physical review B 81: 195406. (2010).
[26]. Lee C., Wei X., Kysar J. K., and Hone J. Measurement of elastic properties and intrinsic strength of monolayer grpahen. Science 321:385. (2004).
[27]. Ni Z. H., Wang H. M., Ma Y., Kasim J., Wu Y. H., and Shen Z. X. tunable stress and controlled thickness modification in graphene by annealing. ACS Nano 2:2301 (2008).
[28]. Liu F., Ming P., and Li J. Ab ignition calculation of ideal strength and phonon instability of graphene under tension. Physical review B 76:064120. (2007).
[29]. Pereira V. M., Peres N. M. R., and Castro Neto A. H. Tight-binding approach to uniaxial strain in graphene. Physical review B 80: 045401 (2009).
[30]. Gao Y., and Hao P. Mechanical properties of monolayer graphene under tensile and compressive loading. Physica E 41: 1561 (2009).
[31]. Xu Z. Graphene nanoribbons under tension. Journal of computational and Theoretical nanoscience 6:625 (2009).
[32]. Scarpa F., Adhikari S., and Srikantha Phani A. Effective elastic mechanical properties of single layer graphene sheets Nanotechnology 20:065709. (2009).
[33]. Y. L. Liu, B. Xie, Z. Zhang, Q. S. Zheng, and Z. P. Xu. Mechanical properties of graphene papers. https://arxiv.org/pdf/1105.0138 (2011).
[34]. Erdongan E., Popov I., Rocha C. G., Cuniberti G., Roche S., and Seifert G. Engineering carbon chains from mechanically streched graphene-based materials. Physical Review B 83:041401(R). (2011).
[35]. Isacsson A. Nanomechanical dipacement detection using coherent transport in ordered and disopdered graphene nanoribbon resonators. arXiv: 1010.0508v1 . (2010).

[36]. Kinder J. M., Dorando J. J., Wang H., and Chan G. K.-L. Perfect reflection of chiral fermions in gated graphene nanoribbos Nano letters 9: 1980-1983. (2009).
[37]. Yu Y. J., Zhao Y., Louis S. R., Kwang E. B., Kim S., and Kim P. Tuning the graphene work function by electric fields. Nano letter 9:3430-3434. (2009).
[38]. Yan J., Zhang Y., Kim P., and Pinczuk A. Electric field effect tuning electron-phonon coupling in graphene. Physical Review Letters 98: 166802. (2007)..
[39]. Landau L. D., and Lifshitz E. M. Quantum Mechanics-third version. Oxford: Pergamon. (1977).
[40]. Jackson J. D. Classical Electrodynamics. New York: Wiley. (1962).
[41]. Nair R. R., Blake P., Grigorenko A. N., Novoselov K. S., Booth T. J., Stauber T., Peres N. M. R., and Geim A. K. Fine structure constant defines visual transparency of graphene. Science 320 1308. (2008).
[42]. T. Stauber, N. M. R. Peres, and A. K. Geim. Optical conductivity of graphene in the visible region of the spectrum. Physics Review B, vol 78, P8 (2008).
[43]. G. L. Klimchitskaya, and V. M. Mostepanenko. Conductivity of pure graphene: Theoretical approach using the polarization tensor. Physics Review B 93,245419 (2016).
[44]. R. Olac-vaw, H. C. Kang, H. Karasawa, Y. Miyamoto, H. Handa, H. Fukidome, T. Suemitsu, M. Suemitsu, and T. Otsuji, Ambipolar behavior in epitaxial graphene based field-effect transistors on Si substrate. Jpn. J. Applied Physics. 49: 06GG01. (2010).
[45]. H. C. Kang, H. Karasawa, Y. Miyamoto, H. Handa , T. Suemitsu, M. Suemitsu, T. Otsuji, Epitaxial graphene field effect transistors on silicon substrates. Solid State Electron. 54:1010-1014. (2010).
[46]. T. Otsuji, H. Karasawa, T. Suemitsu, M. Suemitsu, E. Sano, W. Knap, and V. Ryzhii. Emission of terahertz radiatin from two-dimensional electron systems in semiconductor nano-heterostructures C. R. Physics. 11:421-432. (2010).
[47]. S. Bae, H. Kim, Y. Lee, X. Xu, J. S. Park, Y. Zheng, J. Balakrishnan, T. Lei, Ri, Kim, H. Song, Y. I. Kim, Y. J. Kim, and S. Iijima. “Roll-to-roll production of 30-inch graphene films for transparent electrodes”. Nature Nanotechnology 5(8):574-578 (2010).
[48]. D. Rodrigo, O. Limaj, D. Janner, D. Etezadi, F. J. G. De Abajo, V. Pruneri, and H. Altug. Science. Vol 349. (6244) P165. (2015).
[49]. Eizenberg, M., Blakely, J.M.: Carbon monolayer phase condensation on Ni(111). Surf. Sci. 82(1–2), 228–236 (1979).
[50]. Eizenberg, M., Blakely, J.M.: Carbon interaction with nickel surfaces: monolayer formation and structural stability. J Chem Phys 71(8), 3467 (1979).
[51]. S. A. Bhuyan, N. Uddin, M. Islam, F. A. Bipasha, and S. S. Hossain. Synthesis of graphene. Int. Nano. Lett. Vol 6: 65-83. (2016).
[52]. Lang, B.: A LEED study of the deposition of carbon on platinum crystal surfaces. Surface Science 53(1), 317–329 (1975).
[53]. Novoselov, K.S., Geim, A.K., Morozov, S.V., Jiang, D., Zhang, Y., Dubonos, S.V., Grigorieva, I.V., Firsov, A.A.: Electric field effect in atomically thin carbon films. Science 306(5696), 666–669 (2004).

[54]. Allen, M.J., Tung, V.C., Kaner, R.B.: Honeycomb carbon: a review of graphene. Chem. Rev. 110(1), 132–145 (2010).
[55]. Viculis, L.M., Mack, J.J., Kaner, R.B.: A chemical route to carbon nanoscrolls. Science 299(5611), 1361 (2003).
[56]. Park, S., Ruoff, R.S.: Chemical methods for the production of graphenes. Nat. Nanotechnol. 4, 217–224 (2009).
[57]. Song, L., Ci, L., Gao, W., Ajayan, P.M.: Transfer printing of graphene using gold film. ACS Nano 3(6), 1353–1356 (2009).
[58]. Dikin, D.A., Stankovich, S., Zimney, E.J., Piner, R.D., Dommett, G.H.B., Evmenenko, G., Nguyen, S.T., Ruoff, R.S.: Preparation and characterization of graphene oxide paper. Nature 448, 457–460 (2007).
[59]. Lang B. A LEED study of the deposition of carbon on platinum crystal surface. Surface Science 53 (1): 317-329. (1975).
[60]. Eizenberg M., J. M. Blakely. Carbon monolayer phase condensation on Ni (111). Surface Science 82 (1) :228-236. (1979).
[61]. Somani P. R., S. P. And M. Umeno. Planar nano-graphenes from camphor by CVD. Chemical Physics Letter: 430 (1-3): 56-59. (2006).
[62]. Obraztsov A. N., E. A. Obraztsova, A. V. Tyurnina, and A. A. Zolotukhin. Chemical vapor deposition of thin graphite films of nanomiter thickness. Carbon 45 (10): 10451-10453. (2007).
[63]. Verma V. P., S. Das, I. Lahiri, and W. Choi. Large area graphene on polymer film for flexible and transparent anode in field emission device. Applied physics Lett 96 (20). (2010).
[64]. Drienovsky M, Schrettenbrunner F-X, Liu M-H, Sandner A, Tkatschenko F, Richter K, et al., Towards super lattices: Lateral bipolar multibarriers in graphene, Physical Review B 89, 115421 (2014).
[65]. Dubey S, Singh V, Bhat AK, Parikh P, Grover S, Sensarma R, et al. Tunable superlattice in graphene to control the number of dirac points. Nano Lett;13(9):3990–5. (2013).
[66]. Huard B, Sulpizio JA, Stander N, Todd K, Yang B, Goldhaber- Gordon D. Transport measurements across a tunable potential barrier in graphene. Phys Rev Lett 98:236803. (2007).
[67]. Williams JR, DiCarlo L, Marcus CM. Quantum hall effect in a gate-controlled p-n junction of graphene. Science 317(5838):638–41. (2007).
[68]. Allen M. T., Martin J., Yacoby A. Gate-defined quantum confinement in suspended bilayer graphene. Nat Commun3:934. (2012).
[69]. Velasco J., Jing L., Bao W., Lee Y., Kratz P., Aji V., et al. Transport spectroscopy of symmetry-broken insulating states in bilayer graphene. Nat Nano 7(3):156–60. (2012).
[70]. Weitz RT, Allen MT, Feldman BE, Martin J, Yacoby A. Brokensymmetry states in doubly gated suspended bilayer graphene. Science 330(6005):812–6. (2010).
[71]. Dean C. R., Young A. F., MeriI I., Lee C., Wang L., Sorgenfrei S., Watenabi K., Taniquechi T., Kim P., Shepord K. L., and Hone J. Boron Nitride substrate for high-quality graphene electronics. Nat Nano 5(10):722–6 (2010).

[72]. Sosan C., Kihm K. D., Kim H. G., Lim G., Park J. S., and Lee J. S. How to reliably determine the complex refractive index (RI) of graphene by using two independent measurement constraints. Science Report 4: 6364. (2014).
[73]. Xue, T., Cui X. Q., Chen J. L., liu C., Wang Q., and Zheng W. T. A switch of the oxidation state of graphene oxide on a surface plasmon resonance chip. ACS Appl. Mater. Interfaces 5, 2096–2103 (2013).
[74]. Matkovic, A., Beltaos A., Milic´evic´ M. , Ralevic´ U., Vasic´ B., Jovanovic´ D., and Gajic´ R. Spectroscopic imaging ellipsometry and Fano resonance modeling of graphene. J. Appl. Phys. 112, 123523 (2012).
[75]. Weber, J. W., Calado, V. E. and van de Sanden, M. C. M. Optical constants of graphene measured by spectroscopic ellipsometry. Appl. Phys. Lett. 97, 091904 (2010).
[76]. Bruna, M. and Borini, S. Optical constants of graphene layers in the visible range. Appl. Phys. Lett. 94, 031901–031903 (2009).
[77]. A. Siegman. Lasers (Sausalito, CA: University Science Books, 1986). S. A. Self. "Focusing of Spherical Gaussian Beams." Appl. Opt. 22, no. 5 (March 1983): 658 (1986).
[78]. H. S. Skulason. Optical properties of few and many layer graphene flakes. Master degree thesis, McGill University. (2009).
[79]. Novoselov K. S, Geim A.K, Morozov S. V, Jiang D, Zhang Y, Dudonos S. V, Grigorieva I.V and Firsov A. A. Electric field effect in atomically thin carbon films. Science 306 666-9, (2004).
[80]. A. R. Wright, X. G. Xu, J. C. Cao, and C. Zhang. Strong nonlinear optical response of graphene in terahertz regime. Appl. Phys. Lett., 95(7), (2009).
[81]. S. Cheon, K. D. Kihm, H. G. Kim, G. Lim, J. S Park and J.S.Lee. How to reliably determine the complex refractive index (RI) of graphene by using two independent Measurement constraints. Scientific Report. Nano 21, (2010).
[82]. Z. Q. Li, E. A. Henriksen, Z. Jiang, Z. Hao, M. C. Martin, P. Kim, H.L. Stormer and D. N. Basov. Dirac charge dynamics in graphene by infrared spectroscopy. Nat. Phys. 4 532-5, (2008).
[83]. Z. H. Ni, H. M. Wang, J. Kasim, H. M. Fan, T. Yu, Y. H. Wu, Y. P. Feng, and Z. X. Shen. Graphene thickness determination using reflection and contrast spectroscopy. Nano letters Vol. 7, No.9 (2758-2763), (2007).
[84]. A. Matkovic´, A. Beltaos, M. Milicevic, Uros Ralevic´, Borislav Vasic´, Djordje Jovanovic´, and Rados Gajic´. Spectroscopic imaging Ellipsometry and Fano renascence modeling of graphene. J. Appl. Phys. 112(12), (2012).
[85]. Q. Ye, J. Wang, Z. B. Liu, Z.C. Deng, X. T. Kong, F. Xing, X. D. Chen, W. Y. Zhou, C. P. Zhang, and J.G. Tian. Polarization dependent optical absorption of graphene under total reflection. Appl. Phys. Lett. 102, 021912 (2013).
[86]. T. Xue, X. Q. Cui, J. L. Chen, C. Liu, Q. Y. Wang, H. T. Wang and W. T. Zheng. A switch of the oxidation state of graphene oxide on a surface plasmon resonance chip. ACS Appl. Mater. Interfaces 5, 2096–2103 (2013).
[87]. L. Yang, J. Deslippe, C. H. Park, M. L. Cohen and S. G. Louie, "Excitonic Effects on the Optical Response of Graphene and Bilayer Graphene", Phys. Rev. Lett. 103,

186802 (2009).
[88]. Palik E D. Handbook of Optical Constants of Solids (New York: Academic) third edition. (1998).
[89]. Jellison G E, Hunn J D and Lee H N Measurement of optical functions of highly oriented pyrolytic graphite in the visible Phys. Rev. B 76 085125 (2007).
[90]. Ahuja R, Auluck S, Wills J M, Alouani M, Johansson B and Eriksson O. Optical properties of graphite from first-principles calculations Phys. Rev. B 55 4999–5005 (1997).
[91]. Bruna M and Borini S Optical constants of graphene layers in the visible range Appl. Phys. Lett. 94 031901 (2009).
[92]. M Klintenberg, S Lebegue, C Ortiz1, B Sanyal1, J Fransson1 and O Eriksson. Evolving properties of two-dimensional materials: from graphene to graphite. J. Phys.: Condens. Matter 21, 335502 (2009).
[93]. J. Lindhard, V. Nielsen, M. Scharff, Kongr. D. V. Selsk. Theory of Sputtering. I. Sputtering Yield of Amorphous and Polycrystalline Targets. Mat-fys. Medd. 36, No. 10 (1968).
[94]. Bolotin, K.; Sikes, K. J.; Jiang, Z.; Klima, M.; Fudenberg, G.; Hone, J.; Kim, P.; Stomer, H. L. Ultrahigh electron mobility in suspended graphene. Solid State Commun. **146**, 351-355 (2008).
[95]. G. W. Hanson, "Dyadic Green's functions and guided surface waves for a surface conductivity model of graphene," J. Appl. Phys 103, 064302 (2008).
[96]. G. Xu, R. Lu, J. Liu, H. Chiu, R. Hui, and J. Wu, "Photodetection based on ionic liquid gated plasmonic Ag nanoparticle/graphene nanohybrid field effect transistors," Adv. Opt. Mater. 2, 729–736 (2014).
[97]. X. Wang, Y.P. Chen and D. D. Nolte. " Strong anomalous optical dispersion of graphene: complex refractive index measured by picometrology", Opt. Express 16 22105-12 (2008).
[98]. Z. H. Ni, Y. Y. Wang, T. Yu, and Z. X. Shen, "Raman spectroscopy and imaging of graphene," Nano Res. 1, 273–291 (2008).
[99]. Y. G. Lee, C. G. Kang, U. J. Jung, J. J. Kim, H. J. Hwang, H.-J. Chung, S. Seo, R. Choi, and B. H. Lee, "Fast transient charging at the graphene/SiO2 interface causing hysteretic device characteristics," Appl. Phys. Lett. 98, 183508 (2011).
[100]. Y.-M. Lin, C. Dimitrakopoulos, K. A. Jenkins, D. B. Farmer, H.-Y. Chiu, A. Grill, and Ph. Avouris, "100-GHz transistors from wafer-scale epitaxial graphene," Science 327, 662 (2010).
[101]. F. Schedin, A. K. Geim, S. V. Morozov, E. W. Hill, P. Blake, M. I. Katsnelson, and K. S. Novoselov, "Detection of individual gas molecules adsorbed on graphene," Nat. Mater. 6, 652–655 (2007).
[102]. V. Meera and Girish S. Seltlur. Conductivity tensor of graphene through reflection of microwave measurements. Appl. Phys. 42 055403 (2009).
[103]. B. Semnani, A. H. Majedi and S. Safavi-Naeini. Nonlinear quantum optical properties of graphene. J. Opt. 18 035402 (2016).
[104]. L. Ju, B. Geng, J. Horng, C. Girit, M. Martin, Z. Hao, H. A. Bechtel, X. Liang, A. Zettl, Y. R. Shen, and F. Wang, "Graphene plasmonics for tunable terahertz

metamaterials," Nat. Nanotechnol. 6, 630–634 (2011).
[105]. M. Liu, X. Yin, E. Ulin-Avila, B. Geng, T. Zentgraf, L. Ju, F. Wang, and X. Zhang, "A graphene-based broadband optical modulator," Nature 474, 64–67 (2011).
[106]. Y. Ouyang, Y. Yoon, J.K. Fodor, and J. Guo, Comparison of performances limits for carbon nanoribbon and carbon nanotube transistors. Appl. Phys. Lett., 89, 203107 (2006).
[107]. George W. Hanson. "Dyadic Green's Functions and Guided Surface Waves for a Surface Conductivity Model of Graphene" arXiv:cond-mat/0701205v3 [cond-mat.mtrl-sci] (2008).
[108]. H.-C. Kanga , H. Karasawaa , Y. Miyamotoa , H. Handaa , H. Fukidomea , T. Suemitsu, M. Suemitsu, and T. Otsuji. "Epitaxial Graphene Top-Gate FETs on Silicon Substrates" ISDRS 2009 (2009)
[109]. K.S. Novoselov, A.K. Geim, S.V. Morozov, D. Jiang, M.I. Katsnelson, I.V. Grigorieva, S.V. Dubonos and A.A. Firsov, Two-dimensional gas of massless Dirac fermions in graphene. Nature 438, 197 (2005).
[110]. V. G. Gusunin, S. G. Sharapov, and J, P, Carbotte, Magneto optical conductivity in Graphene. J. Phy.: Condens Matter, 19, 026222(2007).
[111]. Z. Lu and W. Zhao, "Nanoscale electro-optic modulators based on graphene-slot waveguides," J. Opt. Soc. Am. B 29, 1490–1496 (2012).
[112]. B. Semnani, A.H. Majedi and S. Safavi-Naeini. Nonlinear quantum optical properties of graphene. J. Opt. 18 035402 (14pp) (2016).
[113]. J. Liu, G. Xu, C. Rochford, R. Lu, J. Wu, C. M. Edwards, C. L. Berrie, Z. Chen, and V. A. Maroni, "Doped graphene nanohole arrays for flexible transparent conductors," Appl. Phys. Lett 99, 023111 (2011).
[114]. G. Xu, R. Lu, J. Liu, H. Chiu, R. Hui, and J. Wu, "Photodetection based on ionic liquid gated plasmonic Ag nanoparticle/graphene nanohybrid field effect transistors," Adv. Opt. Mater. 2, 729–736 (2014).
[115]. F. Wang, Y. B. Zhang, C. S. Tian, C. Girit, A. Zettl. M. Crommie. Y. R. Shen. "Gated-Variable optical transitions in graphene". Science VOL 320 (2008).
[116]. Y. B. Zhang, Y. W. Tan, H. L. Stormer, P. Kim, Experimental observation of the quatum Hall effect and Berry's phase in graphene. Nature 438, 201 (2005).
[117]. S. Y. Zhou, G. H. Gweon, A. V. Fedorov, P. N. First, W. A. de-Heer, D. H. Lee, F. Guinea, A. H. Carstro Neto, and A. Lezara, Substrate-induced bandgap opening in expitexial graphene Nat. Mater. 6, 770 (2007).
[118]. A. Bostwick, T. Ohta, T. Seyller, K. Horn, E. Rotenberg, Quasiparticle dynamics in graphene. Nat. Phys. 3, 36 (2007).
[119]. S. Y. Zhou, G.-H. Gweon, J. Graf, A. V. Fedorov, C. D. Spataru, R. D. Diehl, Y. Kopelevich, D.-H. Lee, Steven G. Louie, and A. Lanzara., First directly observation of Dirac Femions in graphit.Nat. Phys. 2, 595 (2006).
[120]. X. Wang, Y. P. Chen, and D. D. Nolte, "Strong anomalous optical dispersion of graphene: Complex refractive index measured by picometrology," Opt. Express 16, 22105 (2008).